# ENERGY SCAVENGING USING PIEZOELECTRIC MATERIALS

A thesis presented in partial fulfillment of the

requirements for the degree of

**Master of Engineering**

in

Mechatronics

at

Massey University,

Palmerston North, New Zealand

Huangbo Liang

2008

# Abstract

In recent years, wireless devices have been developing rapidly for various uses that run on batteries. However, when the devices are made smaller and the networks increase in number, it is not practical to replace the depleted batteries, such as in areas difficult to access. Alternative method is to scavenge power available in the environment where the wireless device is placed.

This thesis is focused on scavenging power via vibrations as a power source. According to the literature piezoelectric material is the best choice to convert mechanical forces into electric field. Piezoelectric generator devices have been modelled and analyzed.

A case study of power generator for use in traffic monitoring sensors is assumed. The thesis describes such a piezoelectric power generator, developed based on a cantilever beam and using modelling techniques available in literature. The design is optimized by Sequential Quadratic Programming method. A prototype of the generator is built and tested extensively. The generated power is stored in a specially built circuit.

The experiments show that the prototype piezoelectric power generator can provide 0.09J in a simulated traffic scenario. Also the generated energy can be stored in the electric circuit which gives a stable 5 V DC output. It is noted that piezoelectric material is very brittle and was cracked during the experiment. As a consequence, the most of the experiment were conducted with a slightly modified generator.

In conclusion, this thesis research has developed successfully both mathematical and a physical model of the piezoelectric power generator for wireless traffic monitoring sensors. Further work will still be in order in improving the current design.

# ACKNOWLEDGEMENTS

I wish to express my deepest appreciation and gratitude to my supervisor, Professor Peter Xu, for his supervision, guidance and patience during the course of this project and for helping to solve the problems that have arisen throughout. I would also wish to extend my appreciation to my co-supervisors, Dr Xiang Gui, for his support and invaluable help. I am grateful for all the effort and encouragement provided.

For Mr Bruce Collins of the Electronics Workshop, I would like to thank for his technical assistance, particularly during the circuit design.

And I wish to extend my gratitude to the staff of the mechanical workshop of the ITE, Massey University, Palmerston North, for their assistance.

Finally, I would like to express my special thanks to my mother, father and my wife, Baowei Chen, for their love, encouragement, patience and invaluable help and to my mother in law, Lifang Chen , for looking after my little son well.

# Contents

# 1. Introduction

With the recent advances in wireless and Micro-electro-mechanical-systems (MEMS) technology, the requirement for portable wireless sensors and electronics is growing rapidly. A significant engineering problem that needs to deal with is the supply power for the applications such as medical implants and structural monitoring. The power supply of the applications makes use of the conventional batteries in most cases, however, problems can happen because of their finite lifespan. In some cases, replacing the battery of portable electronics is problematic because the electronics could die at any time. For the wireless sensors application, the sensors can be placed in very remote locations such as structural sensors on a bridge or global positioning system (GPS) tracking devices on animals in the wild. When the battery of all its power goes flat, the sensor must be got back and the battery be replaced. Because these devices are placed in remote locations, only acquiring the sensors and replacing the batteries can become a very expensive task or even impossible. For some civil infrastructure applications the sensors are often expected to be embedded, replacing battery is unfeasible. As an alternative, scavenging energy from the surrounding medium seems very attractive, and then it could be used to replace or charge the battery. One method is to use piezoelectric materials to convert mechanical forces into an electric energy in response to the application of mechanical stresses. This scavenged energy could be used to extend the life of the power supply or in the ideal case provide endless energy for electronic devices lifespan.

The aim of this thesis research was to use piezoelectric material to design and build such a power supply device based on the principle of piezoelectric converter, as proposed by Roundy et al [1]. Then the model of piezoelectric generator was optimized for a wireless magnetic sensor node assumed as the power consumer. This work was carried out with the following objectives:

- *Modelling and analysis of piezoelectric generator.* A general model is formulated for the conversion of the kinetic energy of a vibrating mass to electrical power.
- *Design optimization for wireless sensor node.* A case study of energy scavenging for traffic surveillance is performed and a prototype is

designed and optimized for the wireless traffic sensor node.

- *Circuit design for power storage.* Once the piezoelectric device generated electric power by vibration the circuit is then designed as an energy buffer between the input from the piezoelectric generator and the output to the sensor node.
- *Experimentation of the optimized prototype generator.* A prototype converter is designed and built based on the optimizations. The test results would be presented.

The rest of the thesis is organized as follows. In Chapter Two, literature review is detailed. It focuses on the wireless medical sensor systems and enumerates available power sources for wireless sensor network. In Chapter Three, a brief review of the modelling piezoelectric generator is given first. Then based on the research deduction of Roundy et al [1] a piezoelectric generator is modelled mathematically and simulated for analysis. In Chapter Four, a case study of a wireless magnetic sensor powered by piezoelectric generator is analyzed and the design is optimized in Matlab. In Chapter Five, a circuit for power storage is designed. It is a classical AC-DC converter. In Chapter Six, according to the designed and optimized converter in previous chapter, experiments are conducted and the results analyzed. In Chapter Seven, the conclusions and recommendation are given.

# 2. Literature review

## 2.1. Introduction

Medical monitoring applications have continually developed for decades in healthcare industry. These platforms come with constraints, for example, they may be closed-source platforms or provide service only in limited locations. To achieve a ubiquitous computing environment where patients can be monitored anywhere in the world through wearable sensors and network infrastructures, people have envisioned a wearable sensor system, flexible in its customized configuration to suit unique attributes of each patient. Such a system is able to monitor regular vital signals and generate reports periodically to a server in a medical centre. Physicians in turn are able to query these real-time reports or historical data through medical service networks to provide adequate and correct treatment accordingly. It is also made possible to identify abnormal signals and send out emergency alerts directly. Some emergency situations require instantaneous treatments. Such situations are identified by devices carried by (or implanted in) patients, and treatments are triggered automatically. The modelling of telemedicine is shown in Figure 2-1.

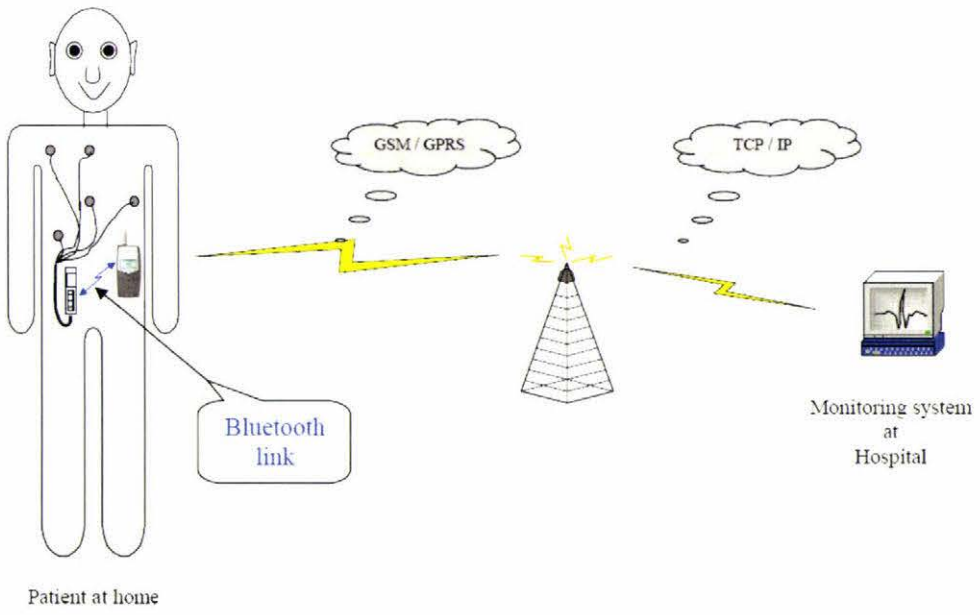


**Figure 2-1: The modelling of Telemedicine [2]**

## 2.2. Wireless medical sensor system

### *2.2.1. Pacemaker*

A pacemaker system consists of three components: a pulse generator and either one or two electrode leads. Pacemakers with one lead are called 'single chamber pacemakers'. Pacemakers with two leads are 'dual chamber pacemakers'. The pacemaker has two parts: the power supply, or batteries, and the electronic circuitry. It is completely covered in metal and sealed to prevent body fluids leaking into the unit. The whole pacemaker weighs only about 20-50g (1-2 ounces) and is smaller than a matchbox. Most pacemakers are powered by lithium batteries. Pacemakers last on average between six and ten years before they need to be replaced [2].

Patient's heart along some small wire leads to a box inserted in the front of a shoulder. From there the box will transmit data to a GSM cellphone. Data from the phone will be beamed via satellite to the database centre before arriving on his/her doctor's cellphone or computer.

### *2.2.2. Electrocardiogram (ECG)*

Traditionally, electrodes with gel have been used. There are problems associated with contact electrodes for long-term ECG monitoring include the necessity to remove hair, the potential loss of contact to the test subject due to drying of application gel or to environmental factors (e.g., sweat) as well as test subject resistance to wearing the electrodes due to discomfort (e.g., skin irritation) [3].

Contemporary ECG system uses standard ECG electrodes which are attached to the LeadWear® System worn by the patient. There are two electronic components: the Patient Transceiver and the Monitor Transceiver. Their functions work as two-way radios that collect and transmit ECG and respiration data to existing bedside or transport ECG monitors. The Patient Transceiver, worn on the patient, communicates with the Monitor Transceiver, placed on or near the ECG monitor. The transceivers are synchronized with a pairing token to establish a secure and robust radio link between the Patient Transceiver and the ECG monitor. The System has also received

approval from the Federal Communications Commission (FCC) to operate using public radio frequencies required for signal transmission [4].

There are 3 components to the system:

- A receiver unit that attaches to a regular monitor via the ECG leads
- A patient unit that is placed on the arm typically.
- A disposable cable (to reduce risk of infection from bacteria that stay on the lead wires) with electrodes.

### *2.2.3. Pulse oxymeter*

A pulse oxymeter combines spectrophotometry to measure hemoglobin concentration (light absorption is a function of the degree of oxygenation) and optical plethysmography to measure pulsatile changes in arterial blood volume and hence heart rate (pulsatile changes in light transmission through living tissue are due to alteration of the arterial blood volume in the tissue) [3].

The measurement is purely based on optical measurements. The sensor placed on a finger, an ear lobe or the forehead has 2 LEDs emitting at 660 nm (red) and 950 nm (near infrared) and a photodetector; in the infrared, the absorption coefficient of oxyhemoglobin is greater than that of reduced hemoglobin. The electronics measure the ratio of pulsatile to non pulsatile light at red and infrared wavelength and translates this ratio to oxygen saturation [3].

The Bluetooth oxymeter can be used with either a finger or an ear probe. This will be evaluated whether it is necessary to incorporate an accelerometer in order to reduce motion artefacts as much as possible. If so, signal processing will need to be developed [3].

### *2.2.4. Blood glucose monitor*

The blood glucose monitor provides wireless transmission of blood glucose readings to a central web-based database, allowing an accurate diary to be kept. This can be easily reviewed by the patient and his physician, with two way wireless messaging

providing insulin schedules, advice and reminders. Expert systems on the server analyze the data and provide immediate feedback to the patient and his doctor. The system facilitates better diabetes management, reducing the long term complications of diabetes [5].

## 2.3. Power sources for wireless sensor networks

### *2.3.1. Introduction*

Currently there are a lot of CMOS circuitries in small size and low power consumption in the world. This leads to heaps of wireless sensors and communication nodes come up. Due to the decrease in size and cost of the wireless sensor, they become widespread in automobiles, buildings, traffic infrastructure, etc. However, because of the prevalence of the wireless, effective power supplies become a larger problem.

The issue is that the decrease in size and cost of CMOS electronics has far exceeded the scaling of energy density in batteries, which are by far the most prevalent power supply currently used. Therefore, the power supply is usually the largest and most expensive component of the emerging wireless sensor nodes being proposed and designed [6]. Moreover, another issue is that the battery power supply limits the lifetime of sensor node. If wireless sensor networks are used widely, the work of replacing batteries for each sensor node for one or two years is very huge and the cost is much expensive.

### *2.3.2. Power consumption*

There are a few low power consumption wireless products that are used commercially and are being developed in the research community. The most common devices currently in the market are based on the Bluetooth standard. A new, lower power, lower data rate standard IEEE 802.15.4 or Zigbee is currently under development.

The power needed to operate these specifications depends on how and where they are used. BlueTooth radios use around 40 – 60 mW. The Zigbee standard aims to cut this

power consumption by a factor of 3. The power consumption of other commercial and academic platforms varies depending on their usage scenarios. Based on the experiment, they generally operate at about 1 order of magnitude lower than BlueTooth which is in the range of 5 – 10 mW depending on the usage environment. Entire power consumption in the specifications is approaching in the hundreds of microwatts [7][8].

### *2.3.3. Comparison of energy scavenging technologies*

There are a lot of infinite energy sources that can be scavenged from the variety of energy sources in the node's environment, i.e.: motion and vibration, air flow, temperature differences, ambient electromagnetic fields, and light and infra-red radiation. Table 2-1 gives the results of a broad survey of potential power sources for wireless sensor nodes, both fixed energy sources such as power scavenging sources. The data are recorded from a combination of published studies, theory, and experiments carried out by the authors [8].

**Table 2-1: Power scavenging sources [8]**

| Power Source | $\mu W/cm^3$ | Secondary Storage Needed | Voltage Regulation |
|---|---|---|---|
| Radioactive | 0.52 | Yes | Yes |
| Solar(outside) | 15000* | Usually | Maybe |
| Solar(inside) | 10* | Usually | Maybe |
| Temperature | 40*# | Usually | Maybe |
| Human Power | 330 | Yes | Yes |
| Air flow | 380## | Yes | Yes |
| Vibrations | 375 | Yes | Yes |

*Denotes sources whose fundamental metric is power per square centimetre rather than power per cubic centimetre.

# Demonstrated from at a 5°C temperature differential.

## Assumes air velocity of 5m/s and 5% conversion efficiency.

### Based on a 1 $cm^3$ closed volume of helium undergoing a 10°C temperature change once per day.

The power sources in above table have a particular level of power generation. Therefore, the lifetime is potentially infinite. All power values are generated by a normalized device size of 1 $cm^3$.

### *A. Radioactive power sources*

Radioactive materials generate radioactive waste, but contain extremely high energy densities. This energy has been used with hydrocarbon fuels on a much larger scale for decades. However, it is not available to power wireless sensor networks because it has not been exploited on a small scale. The radioactive waste can induce a serious health hazard, and is a serious political and controversial issue. Therefore, it is not improved or forbidden the investigation into radioactive power sources. Here it is briefly presented their potential and the research being done in the area.

The total energy emitted by radioactive decay of a material can be expressed as [6].

$$E_t = A_c \cdot E_e \cdot T \qquad (2.1)$$

where $E_t$ is the total emitted energy, $A_c$ is the activity, $E_e$ is the average energy of emitted particles, and T is the time period over which power is collected. Table 4 lists several potential radioisotopes, their half-lives, activity volume density, and energy densities based on radioactive decay. It should be noted that materials with lower activities and higher half-lives will produce lower power levels for more time than materials with comparatively short half-lives and high specific activities. The half-life of the material has been used as the time over which power would be collected. Only alpha and beta emitters have been included because of the heavy shielding needed for gamma emitters. Finally, uranium 238 is included for purposes of comparison only [6].

**Table 2-2 Comparison of radio-isotopes [6]**

| Material | Half-life (years) | Activity volume density ($Ci/cm^3$) | Energy density ($J/cm^3$) |
|---|---|---|---|
| $^{238}U$ | 4.5 × 109 | $6.34 \times 10^{-6}$ | $2.23 \times 10^{10}$ |
| $^{63}Ni$ | 100.2 | 506 | $1.6 \times 10^{8}$ |
| $^{32}Si$ | 172.1 | 151 | $3.3 \times 10^{8}$ |
| $^{90}Sr$ | 28.8 | 350 | $3.7 \times 10^{8}$ |
| $^{32}P$ | 0.04 | $5.2 \times 10^{5}$ | $2.7 \times 10^{9}$ |

***B. Solar Energy***

Based on the research, at midday on a sunny day, the incident light on the earth's surface has a power density of around 100 mW/ $cm^2$. Single crystal silicon solar cells exhibit efficiencies of 15% - 20% under high light conditions, as one would find outdoors. Common indoor lighting conditions have far lower power density than outdoor light. Common office lighting provides about 100 μ W/ $cm^2$ at the surface of a desk. Single crystal silicon solar cells are better suited to high light conditions and the spectrum of light available outdoors. Thin film amorphous silicon or cadmium telluride cells offer better efficiency indoors because their spectral response more closely matches that of artificial indoor light. Still, these thin film cells only offer about 10% efficiency. Therefore, the power is available from photovoltaic ranges from about 15mW/ $cm^2$ outdoors to 10 μ W/ $cm^2$ indoors. A single solar cell has an open circuit voltage of about 0.6 volts. Individual cells are easily placed in series, especially in the case of thin film cells, to get almost any desired voltage needed. A current vs. voltage (I-V) curve for a typical five cell array (wired in series) is shown below in Figure 2-2. Unlike the voltage, current densities are directly dependent on the light intensity [6].

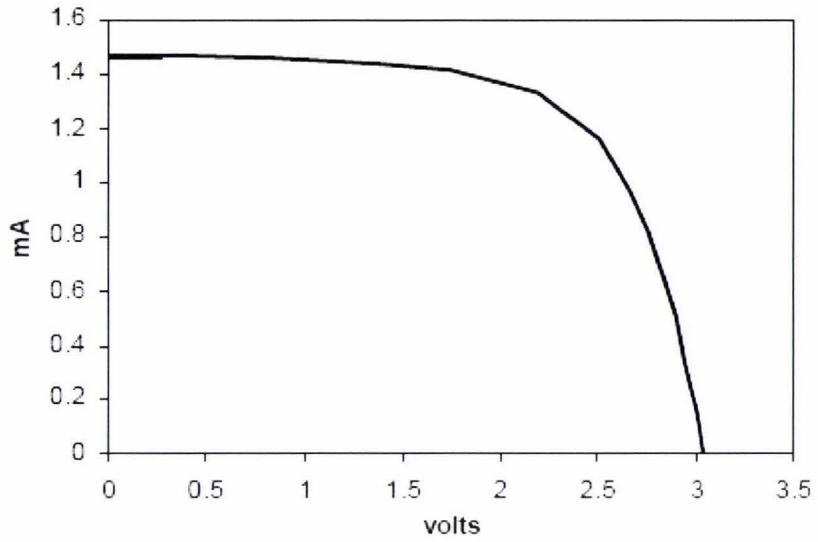


**Figure 2-2: Typical I-V curve from a five cell cadmium telluride solar array [6]**

### *C. Temperature gradients*

Naturally energy can be scavenged from the environment which occurring temperature variations. Stordeur and Stark [9] have demonstrated a thermoelectric micro-device capable of converting 15 μ W/ $cm^3$ from a 10 ° C temperature gradient. With the development of thermoelectrics, this could be improved to more than 15 μ W/ $cm^3$. This device has a static 10 ° C temperature difference within 1 $cm^3$ is very rare. Alternatively, the natural temperature variation over a 24 hour period might be used to generate electricity. It can be assuming an average variation of 7 ° C, that an enclosed volume containing an ideal gas could generate an average of 10 μ W/ $cm^3$. This, however, assumes no losses in the conversion of the power to electricity. In fact some commercially available clocks, such as the Atmos clock, operate on a similar principle. The Atmos clock includes a sealed volume of fluid that undergoes a phase change right around 21 ° C. As the liquid turns to gas during a normal day's temperature variation, the pressure increases the actuating spring that winds the clock. While this is very interesting, the level of power output is still substantially lower than other possible methods [9].

### *D. Passive Human power*

A significant amount of work has been done on the possibility of scavenging power off the human body for use by wearable electronic devices. The conclusion of studies undertaken at MIT suggests that the most energy rich and most easily exploitable source occurs at the foot during heel strike and in the bending of the ball of the foot [10]. This research reported that there will be an average of 330 $\mu W/cm^2$ generated by the piezoelectric shoe inserts while a person is walking. The available power density from the piezoelectric shoe inserts seems suitable for the requirement of the case study in Chapter 4. However, wearable computing and communication devices are not the focus of this project. Moreover, this situation of how to get the energy from a person's foot to other places on the body has not been satisfactorily solved until now. For an RFID tag or other wireless device worn on the shoe, the piezoelectric shoe inserts offer a good solution. However, the application space for such devices is extremely limited, and as mentioned that it is not very applicable to wireless sensor networks.

### *E. Active Human Power*

The type of human powered systems investigated at MIT could be referred to as passive human powered systems where the power is scavenged during common activities rather than requiring the user to perform a specific activity to generate power [1]. Human powered systems of this second type, which require the user to perform a specific power generating motion, are common and may be referred to separately as active human powered systems. Examples include standard flashlights that are powered by squeezing a lever. However active human powered devices are not very applicable for wireless sensor applications at the moment.

### *F. Wind / air flow*

Wind power is quite common to be used as a power source today. The large windmills can be found in many countries. However, there are only few applications

implemented on a small scale which is in a cubic centimetre, generated power from air flow. The available power from wind flow can be easily calculated by [6].

$$P = \frac{1}{2}\rho A \upsilon^3 \tag{2.2}$$

where $P$ is the power, $\rho$ is the density of air, A is the cross sectional area, and $\upsilon$ is the air velocity. Under standard atmospheric conditions, the atmospheric air density is around 1.22 kg/m$^3$. Figure 2-3 shows the power per square centimetre versus air velocity.

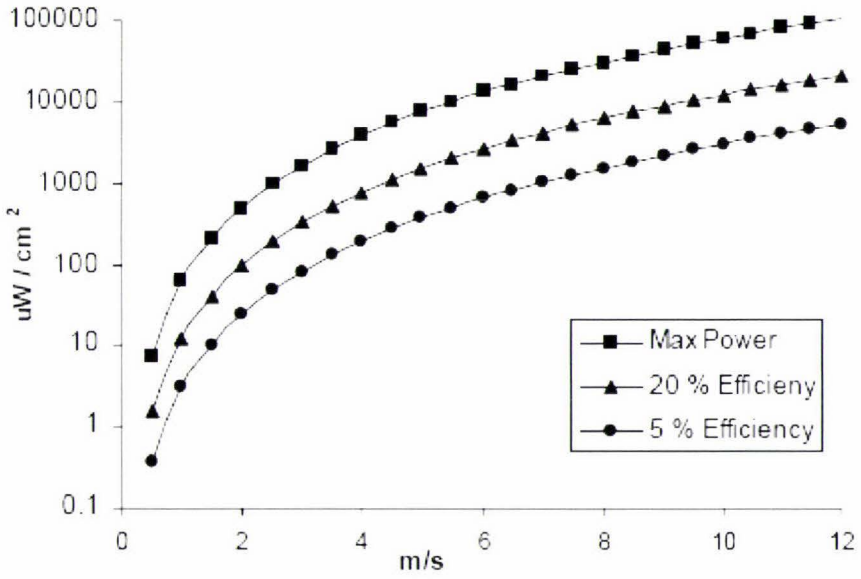


**Figure 2-3 The power per square centimetre versus air velocity [6]**

The large windmills have high efficiencies of about 40%. The efficiencies are dependent on wind velocity, and average operating efficiencies are usually about 20%. Windmills are generally designed when maximum efficiency occurs at wind velocities around 8 m/s or about 18 mph. At low air velocity, efficiency can be significantly lower than 20%. Figure 2-3 also shows power output assuming 20% and 5% efficiency in conversion. As can be seen from the graph, power densities from air velocity are quite useful. As there are many possible applications in which a fairly

constant air flow of a few meters per second exists, it seems that research leading to the development of devices to convert air flow to electrical power at small scales is warranted [6].

### *G. Vibrations*

There are many current applications using low level mechanical vibrations as power sources. Examples include HVAC vents, machine tool, note book computer, exterior windows, wood frame building, washing machine, small household appliances manufacturing and assembly equipment and automobiles. Table 2-3 shows results of measurements on several different vibrations sources. From the table, it can be found that the most peak frequencies of all sources are between 60 and 200 Hz. Acceleration amplitudes range from about 0.1 to 10 $m/s^2$.

**Table 2-3 Vibration sources**

| Vibartion Source | Peak Acc. ($m/s^2$) | Freq. of Peak (Hz) |
|---|---|---|
| HVAC vents in office building | 0.2-1.5 | 60 |
| base of a HP 3-axis machine tool | 10 | 70 |
| Notebook computer while CD is being read | 0.6 | 75 |
| exterior windows in busy street | 0.7 | 100 |
| Second story floor of a wood frame office building | 0.2 | 100 |
| Washing machine | 0.5 | 109 |
| Kitchen blender casing | 6.4 | 120 |
| Clothes dryer | 3.5 | 120 |
| Small microwave oven | 2.25 | 120 |
| Breadmaker | 1.03 | 120 |
| Door frame just after door closes | 3 | 125 |
| Refrigerator | 0.1 | 240 |
| Wooden deck with people walking | 1.3 | 385 |

## 2.4. Conclusion

Based on this survey, temperature variations could only offer the energy scavenging solutions for body wireless sensor networks. A product of Thermo Life Company can interchange heat energy to electrical energy through its thermopile couples using the thermopile principle. If two heat couple plates are connected with a heat source and a heat sink thermally, heat will be converted into electrical energy directly when flowing through thermopiles. Therefore, it's necessary to seek wider solutions for wireless sensor networks. In a word, solar energy and vibrations power were the best ways of supplying for wireless sensor nodes. Both solutions meet the power density requirement in environments that are of interest for wireless sensor networks. The target application of solar power (indoors and outdoors) has to scavenge the power density of solar radiation from the sunshine or lighting. It is not applicable for sensor nodes embedded under ground or hidden place. Therefore, the later chapters focus on the research and development effort on vibration based power generators.

# 3. Modeling and analysis of piezoelectric generator

## 3.1. Introduction

Piezoelectric materials can act as transducers that are able to convert electrical energy to mechanical motion or force, vice versa. Therefore, these materials can be employed to supply power for other devices by changing environmental motion into electrical energy that can be saved and used. Once the power generator absorbing energy is working, the portable devices will not rely on the traditional power supplies, such as the batteries which have limited operational lifespan. "Analytical modeling is an inevitable element in the design process to understand various interrelated parameters and to optimize the key design parameters while studying and implementing such power harvesting devices" [12].

A lot of studies, experiments and patents have been done and report that it is possible to use piezoelectric material devices as power sources. Umeda et al [13] were one of the pioneers to transform mechanical impact energy to electrical power by using a free-falling ball to impact a plate with piezoceramic wafer attached to its underside and developed an electrical equivalent model of the PZT. They also researched the power storage circuit and pointed out its characteristics of composition of the PZT, a bridge rectifier and a capacitor. Starner [14] investigated that the energy can be scavenged from leg motion of a human being and explores mechanical energy from human motion sources, such as blood pressure. The author indicates it is possible to generate around 8.4 watts from a shoe with a mounted PZT. Kymissis et al [15] studied powering up a bulb mounted in a shoe by harvesting energy from walking motion. Kimura's US Patent [16] places a PZT material on the vibration of a small plate and generated a rectified voltage signal. This experiment shows that migratory birds embedded with PZT can provide enough power for a small mounted transmitter to send their code and location. The author also provides a comparison of the result of the experiment and current existing battery technology. Goldfarb et al [17] introduced a linearized model of a PZT stack and analyzed the efficiency of it as a power generation device. The authors claimed that the maximum efficiency is that the devices work in a low frequency source and exciting in fundamental resonance of the stack. The efficiency has a strong relation with the amplitude of the input force due to

hysteresis of the PZT. Clark and Ramsay [18] have found the transverse force ($d_{31}$ mode) in addition to the force applied in the poling direction ($d_{33}$ mode) and compared them. The experiment presented that the d31 mode has a better energy conversion when applying pressure of working stress for power generation. They concluded that the MEMS device can be powered up by a $1cm^3$ piezoceramic wafer in the microwatt range. Elvin et al [19] have done experiments and theoretically studied on using polyvinylidene fluoride (PVDF) to provide power for the wireless sensors. In order to monitor human bone strain, they applied half-rectified circuit combined with wireless communication device. Kasyap et al [20] provided an equivalent circuit of the system as a model to describe the power harvested from the input vibration of a PZT patch attached. They have experimented and obtained a result of the peak power efficiencies of about 20% when using a beam structure. Gonzalez et al [21] studied the future of energy conversion using piezoelectric and provided several suggestions to improve output power of the existing prototypes to the level that can be theoretically obtained. Smits and Chio [22] utilized internal energy conservation theory to describe the electromechanical characteristics of a heterogeneous piezoelectric bender under various electrical and mechanical boundary conditions. However, they did not provide any formulation for the power generation. Roundy et al [1] described the PZT cantilever beam in a different way based on the electrical equivalent circuit, which leads to fair matches with the experimental results.

Some of the above studies have had success in modeling the PZT cantilever beam for voltage and power generation. A bimorph bender has the advantage that it can easily be designed with lower stiffness so that higher strains can be generated with a given force input. In this paper, special emphasis has been given to the optimization of modeling of a bimorph PZT bender with a proof mass in the generator mode. Thus, a new case study is assumed and has been optimized based on the equations Roundy et al provided.

In the following sections of the chapter the various works on power harvesting are broken into the following groups: fundamentals of piezoelectric converter, material selection, mathematical modeling, analysis of model for piezoelectric generator and conclusion. In section 3.2, the mechanical and electrical behavior of a piezoelectric is modeled. In section 3.3, comparison of different material properties is discussed. In

section 3.4, a mathematical modeling will be given based on Roundy et al research. Section 3.5 will give the analysis of model for piezoelectric power generation and discussed the relationships of output power and mechanical damping ratio, electrical damping ratio, input frequency and load resistance. In section 3.6 will give the summaries of the material selection and certain functional relationships.

### 3.2. Fundamentals of piezoelectric converter

Piezoelectric materials are materials that physically deform in the presence of an electric field, or conversely, produce an electrical charge when mechanically deformed. The constitutive equations for a piezoelectric material are given in Eq. (3.1) and (3.2).

$$\delta = \sigma / Y + dE \tag{3.1}$$

$$D = \epsilon E + d\sigma \tag{3.2}$$

Where $\delta$ is mechanical strain, $\sigma$ is mechanical stress, Y is the modulus of elasticity (Young's Modulus), d is the piezoelectric strain coefficient, E is the electric field, D is the electrical displacement, $\epsilon$ is the dielectric constant of the piezoelectric material.

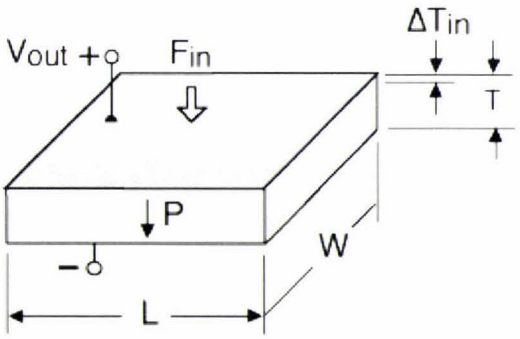


**Figure 3-1 Illustration of 33 mode operation of piezoelectric material [23]**

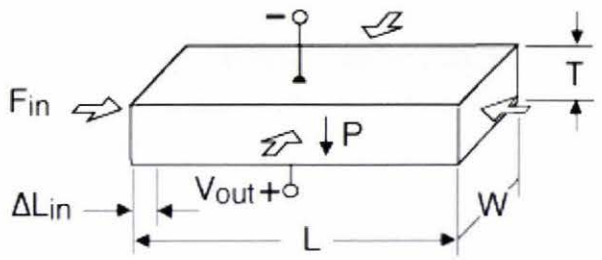


**Figure 3-2 Illustration of 31 mode operation of piezoelectric material [23]**

Figure 3-1 and 3-2 illustrate the two different modes in which piezoelectric material is generally used. Typically, piezoelectric material is used in the d33 mode, meaning that longitudinal generator is compressed from the top and bottom. However, the material can also be operated in the d31 mode, meaning that transverse generator is compressed from the sides. Piezoelectric d31 mode sensors and actuators have a cantilever beam structure that consists of a membrane film, bottom electrode, piezoelectric film, and top electrode. The d31 mode devices require many mask steps (3~5 masks) for patterning of each layer while have very low induced voltage. A generated open circuit voltage (V) can be induced between the electrodes through an applied, external stress (F) and is expressed by [23].

$$V = \frac{Fg_{31}}{W} \tag{3.3}$$

where $g_{31}$ (unit is V·m/N) is the transverse piezoelectric coefficient and $W$ is the width of the PZT thin film.

In the d33 mode a generated open circuit voltage (V) can be induced by external stress (F) due to the longitudinal, piezoelectric coefficient as demonstrated in Eq. (3.4).

$$V = \frac{Fg_{33}T}{LW} \tag{3.4}$$

where $T$ is the thickness of the PZT film and L is the length of the cantilever beam. The magnitude of the g33 is 2 to 2.5 times larger than its g31 counterpart.

Although the electrical/mechanical coupling for the d31 mode is lower than for the d33 mode, there is a key advantage to operating in the d31 mode. The system is much more compliant, therefore larger strains can be produced with smaller input forces. Also, the resonant frequency is much lower. An immense mass would be required in order to design a piezoelectric converter operating in the d33 mode with a resonant frequency somewhere around 25 Hz. Therefore, the use of bending elements operating in d31 mode is essential in this case.

### 3.3. Material selection

Piezoelectric materials create electrical charge when mechanically stressed. Among the natural materials with this property are quartz, human skin, and human bone, though the latter two have very low coupling efficiencies. Table 3-1 shows properties of common industrial piezoelectric materials: lead zirconate titanate (PZT), PVDF and lead zinc niobate-lead titanate (PZN-PT).

**Table 3-1 Comparison of piezoelectric materials [6]**

| Property | Units | PZT | PVDF | PZN-PT |
|---|---|---|---|---|
| Strain coefficient ($d_{31}$) | $10^{-12}$m/v | 320 | 20 | 950 |
| Strain coefficient ($d_{33}$) | $10^{-12}$m/v | 650 | 30 | 2000 |
| Coupling coefficient ($k_{31}$) | CV/Nm | 0.44 | 0.11 | 0.5 |
| Coupling coefficient ($k_{33}$) | CV/Nm | 0.75 | 0.16 | 0.91 |
| Dielectric constant | $\varepsilon/\varepsilon_0$ | 3800 | 12 | 4500 |
| Elastic modulus | $10^{10}$N/m$^2$ | 5 | 0.3 | 0.83 |
| Tensile strength | $10^7$/m$^2$ | 2 | 5.2 | 8.3 |

The piezoelectric strain coefficient (d) relates strain to electric field. The coupling coefficient (k) is an indication of the material's ability to convert mechanical energy to electrical energy or vice versa. It is functionally related to the strain coefficient by

$$K = \sqrt{\frac{Yd}{\varepsilon}} \qquad (3.5)$$

It is clearly seen that materials with larger strain and coupling coefficients have a higher potential for energy conversion. The most efficient energy conversion, as indicated by the coupling constants in Table 3-1, comes from compressing d33 mode. Two other material properties in equation 3.5 are also important. They are the dielectric constant ( $\varepsilon$ ) and the elastic, or Young's, modulus (Y). A higher dielectric constant is generally preferable because it lowers the source impedance of the generator, and piezoelectric materials often have high impedance resulting in higher voltage and lower current output. The elastic modulus primarily affects the stiffness of the bender. Generally, the other material properties are more important for power conversion, and the system can be designed around the stiffness. Finally, the tensile strength of the material is very important. In certain cases, the design will be limited by the maximum strain that a bender can withstand. In these cases, a material with a higher tensile strength would be preferable.

PZT (Lead Zirconate Titanate) is probably the most commonly used piezoelectric material at current time because of its good piezoelectric properties. PVDF (Polyvinylidene Difluoride) is a piezoelectric polymer that is attractive for some applications because of its higher tensile strength and lower stiffness. Commercial applications of piezoelectric devices abound, for instance in speakers, spark generators inside electronic igniters, strain sensors pressure gages and as presice time-keepers in electronic clocks. A few types of basic piezoelectric devices include crystals, tubes, unimorphs, bimorphs and stacks.

Piezoelectric crystals involve a non-uniform charge distribution within the unit cell of the crystal. When exposed to an electric field, this charge distribution shifts and the crystal will change its shape. The same polarization mechanism can cause a voltage to develop across the crystal in response to mechanical force.

Piezoelectric tubes benefit to control an object in space [24]. By sectioning the surface of a tube into four regions and connecting them, as well as one end of the tube to electrodes, it becomes possible to apply voltages to the tube in various directions. By applying voltages perpendicular to the tubes cross-section, it becomes possible to control the position of one end of the tube in two dimensions (x and y), while

applying a voltage along the length of the tube, it becomes possible to control the position in the third dimension (z).

It is very small that the force and displacement created by a pure piezoelectric material so that methods have been developed to allow amplification of the piezoelectric effect. A unimorph is to apply a thin layer of a piezoelectric material to a layer of inactive material. When the piezo expands or contracts, the device will then bend in response.

By combining more than one piezo, it becomes possible to further increase the amount of transduction. For instance, an elongating, bending or twisting device can be created by placing two layers of piezoelectric material on top of one-another, and by controlling the polarization direction and the voltages such that when one layer contracts, the other will expand. Such a device is known as a bimorph.

By stacking of piezo materials into layers, it becomes possible to combine their displacement to create what is known as a piezo stack. Such devices are capable of higher displacements and larger forces [23].

PZN-PT (Lead Zinc Niobate – Lead Titanate) is a single crystal piezoelectric material much likes PZT. It has excellent properties, however, it has just become available commercially. It is very expensive and only very small crystals that can currently be produced. Based on this comparison of piezoelectric materials, PZT has been chosen as the primary material for further development and bimorph structure is used for simulation, prototyping and testing. In this case, the metal centre shim adds strength to the bender and makes it much easier to cut and solder because of the brittleness of the piezoelectric ceramic. Table 3-2 shows the properties of PZT purchased from Piezo Systems Company.

**Table 3-2 Properties of PZT purchased**

| PZT PROPERTY | VALUE |
|---|---|
| Size | 72.4mm ×72.4mm |
| Thickness | 0.267mm |
| Capacitance | 610 nF |
| Dielectric Constant ($\varepsilon/\varepsilon_0$) | 3800 |
| Strain coefficient ($d_{33}$) | $650\times10^{-12}$ meters/volt |
| Strain coefficient ($d_{31}$) | $320\times10^{-12}$ meters/volt |
| Piezoelectric Strain density Coefficient ($g_{33}$) | $19\times10^{-3}$ volts/Newton meter |
| Piezoelectric Strain density Coefficient ($g_{31}$) | $9.5\times10^{-3}$ volts/Newton meter |
| Coupling coefficient($k_{33}$) | 0.75 |
| Coupling coefficient($k_{31}$) | 0.44 |
| Elastic or Young's modulus ($Y_3$) | $5\times10^{10}$ Newtons/meter$^2$ |
| Elastic or Young's modulus ($Y_1$) | $6.2\times10^{10}$ Newtons/meter$^2$ |

## 3.4. Mathematical modelling

### *3.4.1. Vibration-to-electricity conversion model*

A general model for the conversion of the kinetic energy of a vibration with mass to electricity based on the schematic in Figure 3-3 has been proposed by Williams and Yates [11]. This model is described by equation 3.6.

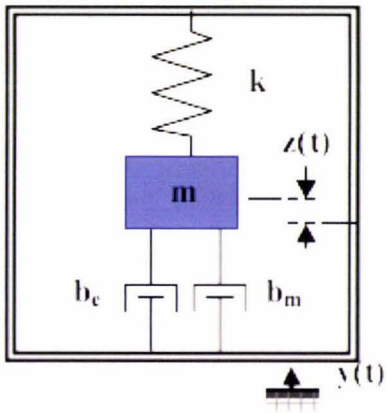


**Figure 3-3 Schematic of generic vibration converter [1]**

$$P = \frac{m\varsigma_e A^2}{4\omega(\varsigma_e + \varsigma_m)^2} \tag{3.6}$$

Where $P$ is the power output, $m$ is the vibration proof mass, $A$ is the acceleration magnitude of the input vibrations, $\omega$ is the frequency of the driving vibrations, $\varsigma_m$ is the mechanical damping ratio, and $\varsigma_e$ is an electrically induced damping ratio. In Eq. (3.6), the maximum power output occurs when the frequency of the driving vibrations matches the fundamental frequency of the vibrating device. Normally the equation is the simple way to roughly estimate the available power output from a vibration source. It is obvious that there are three interesting relationships that are shown below.

- The output power is directly proportional to the vibration proof mass.
- The output power is directly proportional to the square of the acceleration amplitude of the driving vibrations.
- The power output is inversely proportional to input frequency.

The three relationships demonstrate that the device should be designed with heavy mass and placed into a place with low frequency from a vibration source which has a higher acceleration magnitude. Roundy et al have done many measurements on spectra and indicated that in general the lowest frequency peak has the highest acceleration magnitude [1].

### *3.4.2. Modeling piezoelectric elements*

Before modelling piezoelectric elements the geometric terms for bimorph mounted as a cantilever shown in Figure 3-3, it is necessary to provide the details of the derivation of the analytical model for a piezoelectric vibration-to–electricity converter. The piezoelectric bender is a composite beam so that effective moments of inertial and elastic modulus are used. The effective moment of inertia is given by [1].

$$I = 2 \cdot \left[ \frac{wt_c^3}{12} + wt_c b^2 \right] + \frac{Ywt_{sh}^3}{12Y_{sh}} \tag{3.7}$$

$$b = \frac{t_c + t_{sh}}{2} \tag{3.8}$$

where w is the width of the beam, tc is the thickness of an individual piezoelectric ceramic layer, b is the distance from the centre shim to the centre of the piezo layers, $t_{sh}$ is the thickness of the centre shim, and Y is Young's modulus for the piezoelectric ceramic and $Y_{sh}$ is Young's modulus for the centre shim.

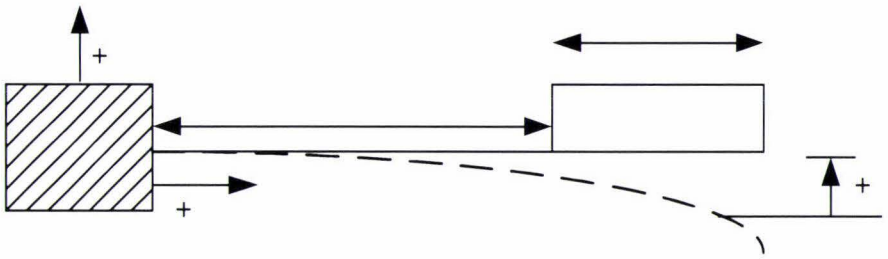


**Figure 3.4 Schematic of piezoelectric bender**

The moment in the beam as a function of the distance x from its base, M, is given by equation 3.9.

$$M = m(\ddot{y} + \ddot{z})(l_b + 0.5l_m - x) \tag{3.9}$$

where $l_m$ is the length of the mass, $\ddot{y}$ is the input vibration in terms of acceleration, $l_b$ is the length of the cantilever beam and $\ddot{z}$ is the vertical acceleration of the beam at the point where the mass attaches with respect to the base of the beam.

The stress and strain values of interest, and those used as state variables are the average of the stress and strain in the piezoelectric material that is covered by an electrode. An expression for the average of the stress in the piezoelectric material covered by the electrode is given by,

$$\sigma = m(\ddot{y} + \ddot{z})\frac{b(2l_b + l_m - l_c)}{2I} \tag{3.10}$$

Therefore, b` is defined below.

$$b' = \frac{2I}{b(2l_b + l_m - l_c)} \tag{3.11}$$

In addition, applying Euler beam yields,

$$\frac{d^2z}{dx^2} = \frac{M(x)}{YI} \tag{3.12}$$

At the point where the beam meets the mass integrating to obtain an expression for the deflection term ($z$) yields:

$$z = \frac{m(\ddot{y} + \ddot{z})l_b^2}{2YI} \cdot \left(\frac{2}{3}l_b + \frac{1}{2}l_m\right) \tag{3.13}$$

Finally, realizing that strain is equal to stress over the elastic constant, $\delta = \sigma / Y$, and that stress can be expressed as in equation 3.10, strain can be written as shown below:

$$\delta = \frac{m(\ddot{y} + \ddot{z})b}{2YI} \cdot (2l_b + l_m - l_c) \tag{3.14}$$

Substituting Eq. (3.13) into equation 3.12 yields:

$$\frac{\delta}{z} = \frac{3b(2l_b + l_m - l_c)}{l_b^2(2l + 1.5l)} \tag{3.15}$$

Defining $b^* = \delta / z$, so the equation was written as below:

$$b^* = \frac{3b(2l_b + l_m - l_e)}{l_b^2(2l + 1.5l)} \tag{3.16}$$

A convenient method of modelling piezoelectric elements is to model both the mechanical and electrical portions of the piezoelectric system as circuit elements. The equivalent circuit of piezoelectric material is modelled by the equivalent circuit parameters derived from the complex materials coefficients which are connected to real and imaginary parts of the complex materials coefficients of the piezoelectric device. The equivalent circuit parameters are measured in temperature and stress experiments. As a result, the piezoelectric coupling is then modelled as a transformer and the mass attached to the end of the cantilever beam is shown as an inductor [24]. Figure 3-5 shows the circuit model of the piezoelectric element

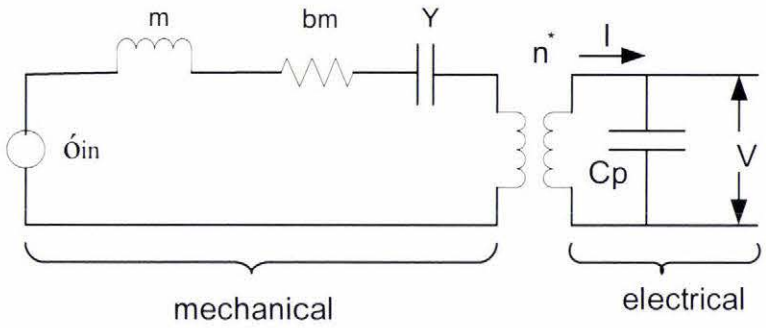


**Figure 3-5 Circuit model of the piezoelectric element**

The across variable on the electrical side is voltage (V) and the through variables current (I). The across variable on the mechanical side is stress (σ) and the through variable is strain (δ). The system equations can then be obtained by simply applying Kirchoff's Voltage Law and Kirchoff's Current Law. However, first the stress / strain relationships for circuit elements on the mechanical side need to be defined.

$\sigma_{in}$ is an equivalent input stress. In other words, it is the stress developed as a result of the input vibrations. m, shown as an inductor, represents the effect of the mass, or inertial term. The stress "across" this element is the stress developed as a result of the mass flexing the beam. Thus, the relationships for the input element, $\sigma_{in}$, and the inertial element, m, are given as follows,

$$\sigma_{in} = \frac{m}{b'} \ddot{y} \tag{3.17}$$

$$\sigma_{m} = \frac{m}{b^* b'} \ddot{\delta} \tag{3.18}$$

where $\ddot{y}$ is the input vibration in terms of acceleration.

The resistive element in Figure 3-5 represents damping, or mechanical loss. The damping coefficient, $b_m$, relates stress to tip displacement, z. The stress relationship for the damping element, $b_m$, becomes:

$$\sigma_{bm} = \frac{b_m}{b^*} \cdot \dot{\delta} \tag{3.19}$$

$C_e$ is the capacitance of the bimorph. The vibration input is shown as a stress generator ($\sigma_{in}$), which comes from the input acceleration $A_{in}$. The relationship between the input vibrations and an equivalent stress input is:

$$\sigma_{in} = \frac{m}{b} \cdot A_{in} \tag{3.20}$$

The transformer relates stress (σ) to electric field (E) at zero strain, or electrical displacement (D) to strain (δ) at zero electric field. So the equations for the transformer are:

$$\sigma = -YdE \tag{3.21}$$

$$D = -dY\delta \tag{3.22}$$

The equivalent ratio (n*) for the transformer is dY. Note that voltage V = 2Etc, Q = $l_e$wD. Then the equations for the transformer can be rewritten as:

$$\sigma_t = \frac{-dY}{2t_c} \cdot V \tag{3.23}$$

$$Q = -dYl_e w\dot{\delta} \tag{3.24}$$

Applying Kirchoff's Voltage Law to the circuit in Figure 3-5 yields the following equation:

$$\sigma_m = \sigma_m + \sigma_{bm} + \sigma_t \tag{3.25}$$

Substituting Eq. (3.17), (3.18), (3.19), and (3.23) and rearranging terms yields the third order equation shown as 3.26, which describes the mechanical dynamics of the system with an electrical coupling term.

$$\ddot{\delta} = -\frac{Yb^*b'}{m}\delta - \frac{b_m b'}{m}\dot{\delta} + \frac{dY}{2t_c}\frac{b^*b'}{m}V + b^*\ddot{y} \tag{3.26}$$

The capacitance of the piezoelectric bender can be computed in Eq. (3.27).

$$C = \frac{\varepsilon L w}{T} \tag{3.27}$$

where $L$ is the length of the bender, w is the width of the bender, $T$ is the thickness of the bender, $\varepsilon$ is the static permittivity of PZT. Note that $C = \frac{Q}{V}$, substituting the Eq. (3.24) and rearranging terms yields Eq. (3.28).

$$\dot{V} = \frac{-2dYt_c}{\varepsilon} \cdot \dot{\delta} \tag{3.28}$$

Figure 3-5 is an open circuit, so there is no power is transferred. It is necessary to consider there is a resistor is used as the load. This results in the circuit model shown in Figure 3-6.

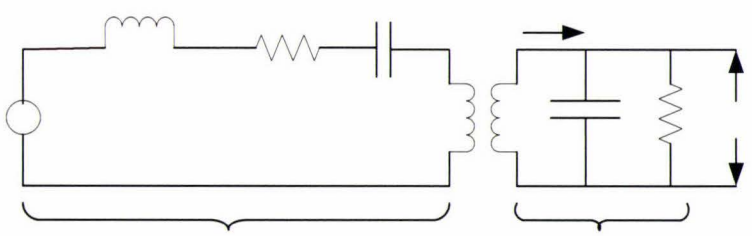

**Figure 3-6 Circuit model of the piezoelectric element**

Therefore, according to Kirchoff's Voltage Law and Kirchoff's Current Law, the equivalent electrically induced damping ratio is given by the expression,

$$\zeta_e = \frac{\omega k^2}{\sqrt{\omega^2 + 1/(RC)^2}} \tag{3.29}$$

where k is the piezoelectric coupling coefficient, R is the load resistor, C is the capacitance of the piezoelectric bender.

Applying Kirchoff's Current Law to the electrical side of the circuit now yields the following equation, which replaces Eq. (3.28) in the system model.

$$\dot{V} = -\frac{2Ydt_c}{\varepsilon}\delta - \frac{1}{RC}V \tag{3.30}$$

Taking the Laplace transform of equation 3.30 and rearranging terms yields the following expression:

$$\Delta = -\frac{\varepsilon}{2Ydts}\left(s + \frac{1}{RC}\right)\cdot V \tag{3.31}$$

where $\Delta$ is Laplace transform of strain ($\delta$) and s is the Laplace variable.

Taking the Laplace transform of Eq. (3.26) and rearranging terms yields:

$$\Delta\left(s^2 + \frac{b_m b'}{m}s + \frac{Yb^* b'}{m}\right) = \frac{Yb^* b' da}{2mt_c}V + b^* A_{in} \tag{3.32}$$

Substituting Eq. (3.31) into (3.32) then the output voltage can be solved in following expression:

$$V\left\{s^3 + \left(\frac{1}{RC} + \frac{b_m b'}{m}\right)s^2 + \left[\frac{Yb^* b'}{m}\left(1 + \frac{d^2 Y}{\varepsilon}\right) + \frac{b_m b'}{mRC}\right]s + \frac{Yb^* b'}{mRC}\right\} = -\frac{2Ydtb^*}{a\varepsilon}A_{in} \tag{3.33}$$

Note that $d^2Y/\varepsilon$ is the square of a term commonly referred to as the piezoelectric coupling coefficient denoted by the symbol *k*, the Laplace variable may be substituted

with $jw$ where $j$ is the imaginary number, $Yb^*b'/m$ is the natural frequency of the system represented by the symbol $\omega_n$, and the damping term $b_m b'/m$ can be rewritten in terms of the damping ratio $\zeta$ as $2\zeta\omega_n$. The new expression is given in Eq. (3.34).

$$V = \frac{-jw\dfrac{2Ydt_c b^*}{a\varepsilon}}{\dfrac{1}{RC}\omega_n^2 - \left(\dfrac{1}{RC} + 2\zeta\omega_n\right)\omega^2 + j\omega\left[\omega_n^2(1+k^2) + \dfrac{2\zeta\omega_n}{RC} - \omega^2\right]} A_{in} \tag{3.34}$$

By proper selection of the load resistance (R), $\zeta_e$ will be equal to the mechanical damping ratio $\zeta_m$. In addition, if it is assumed that the frequency of the input vibrations (ω) is equal to the undamped natural of the device ($\omega_n$), the analytical expression for power transferred to the load is given in Eq. (3.35) [1].

$$P = \frac{V^2}{2R} = \frac{1}{(\omega\varepsilon)^2} \cdot \frac{RC^2(Y_c dt_c b^*)^2}{(4\zeta^2 + k^4)(RC\omega)^2 + 4\zeta k^2(RC\omega) + 2\zeta^2} A_{in}^2 \tag{3.35}$$

where $t_c$ is thickness of one piezoelectric layer, b* is the geometric constant relating average strain to displacement at the beam's end, $A_{in}$ is the acceleration magnitude of input vibrations.

### 3.5. Analysis of model for piezoelectric power generator

Once the expression for output power of the piezoelectric generator is specified, the relationship between the output power and variables are analytical. The variables of the initial prototype and model are shown in Table 3-3.

**Table 3-3 Variables of initial model**

| Variables | Description |
|---|---|
| $l_m$ | Length of the mass |
| $h_m$ | Height of the mass |
| $w_m$ | Width of the mass |

| | |
|---|---|
| $l_b$ | Length of the cantilever beam |
| $w_b$ | Width of the cantilever baem |
| $l_e$ | Length of the electrode on the beam surface |
| $t_p$ | Thickness of one piezoelectric layer |
| $t_{sh}$ | Thickness of the center shim |
| $R_L$ | Load resistance |

This cantilever mechanically resonates at a natural frequency, just like anything that vibrates has a natural frequency. The piezoelectric bender mounted as a cantilever beam as shown in Figure 3-7.

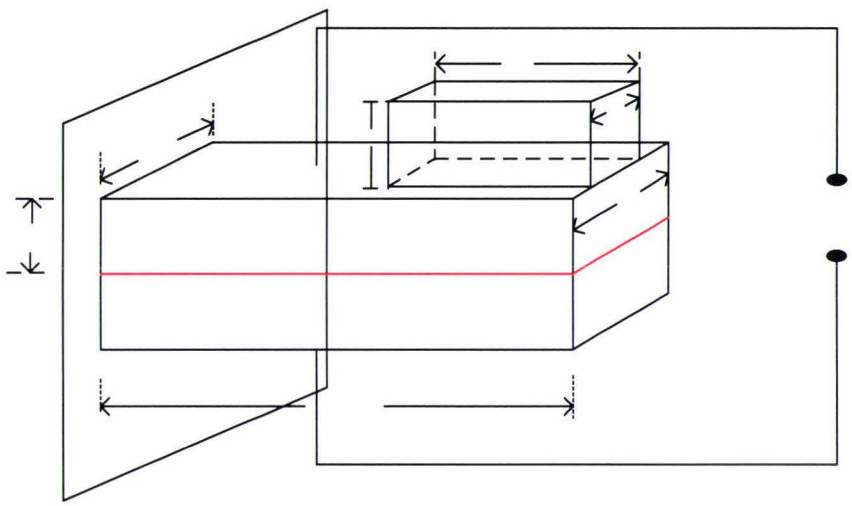

**Figure 3-7 Cantilever beam with piezoelectric material**

le is not shown in the figure and is always equal to or less than the length of the beam. The beam consists of a centre shim and two layers of piezoelectric material. Each layer is assumed to be homogeneous. The metal centre shim makes the bender more reliable due to the brittleness of the piezoelectric ceramic. The natural frequency of the cantilever beam can be computed using the formulas developed for homogeneous beams given below,

$$F_{natural} = \frac{1}{2\pi} \cdot \sqrt{\frac{3YI}{ML^3}} \tag{3.35}$$

where I is the area moment of inertia of beam, L is the span of beam, M is mass and Y is Young's modulus. It is assumed that the frequency of the driving vibration is exactly equal to the natural frequency of the cantilever. Then, Eq. (3.35) can give the output power for the power conversion.

It is not obvious to find the relationship between the proof mass and the output power Eq. (3.35). However, geometric strain constant b* is the middle character interacting the result from the expression. The geometric strain constant is given by Eq. (3.16).

Actually the output power is proportional to the proof mass. In order to maintain the same resonant frequency, if the mass increases, either the thickness or the width of the beam must increase as well. If the thickness increases, $t_c$, b and b* will increase, resulting in a higher output power. If the width increases, the capacitance of the piezoelectric bender C will go up, getting a higher output power as well.

It is assumed that the total volume of the bimorph and mass is approximately $1cm^3$. According to the Table 2-2, in order to simulate a vibration source related to street/road environment for further study, a window close to busy street was assumed as the vibration sources, so the peak frequency of 100 Hz and peak acceleration of 0.7 $m/s^2$ were applied for all the simulations.

### 3.6. Simulation of initial model

It is obvious that the power output is inversely proportional to the mechanical damping ratio. This follows from Eq. (3.35). It should be noted that if the equivalent electrically induced damping ratio $\zeta_e$ is equal to the mechanical damping $\zeta_m$ in the system, maximum output power will occur. Figure 3-8 shows the simulated power output vs. the mechanical damping ratio.

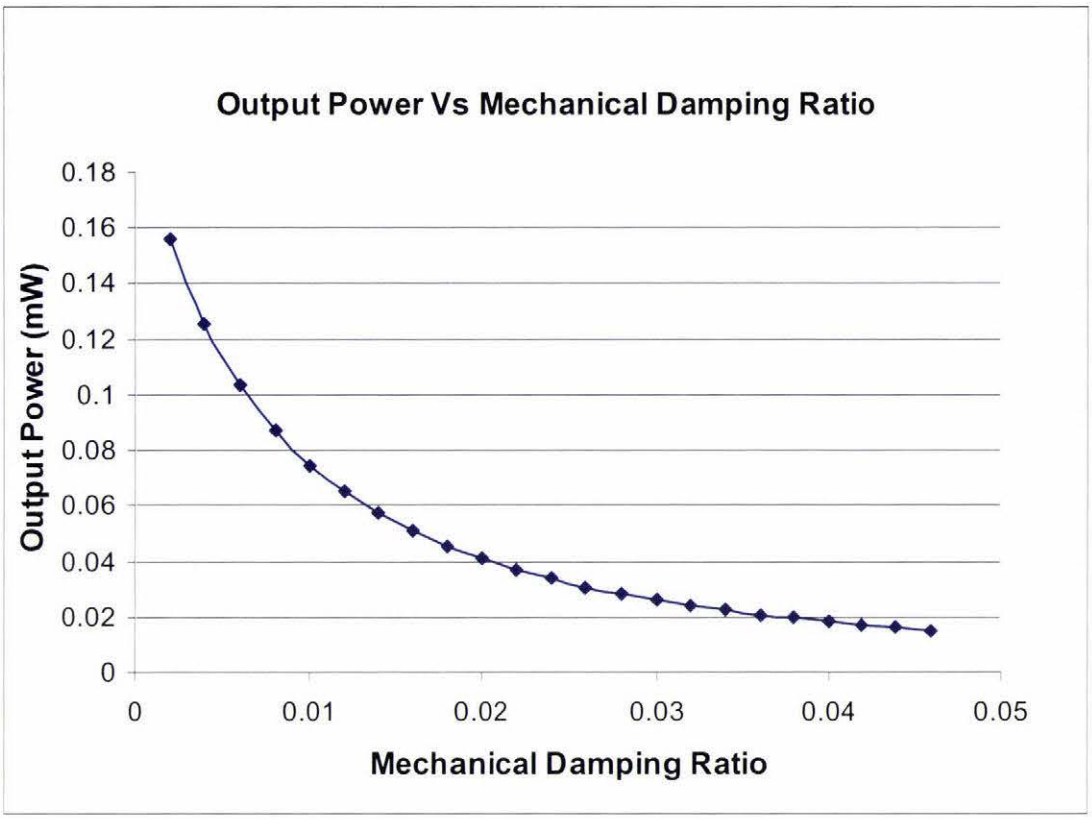


**Figure 3-8 Output power versus mechanical damping ratio**

The term $\zeta_e$ represents an electrically induced damping coefficient. It is generally a function of circuit parameters. The output power is maximized when $\zeta_e$ and $\zeta_m$ are equal, and they are as low as possible. Figure 3-9 shows that $\zeta_e$ is equal to $\zeta_m$ around 0.02 and the output power is 40.8μW.

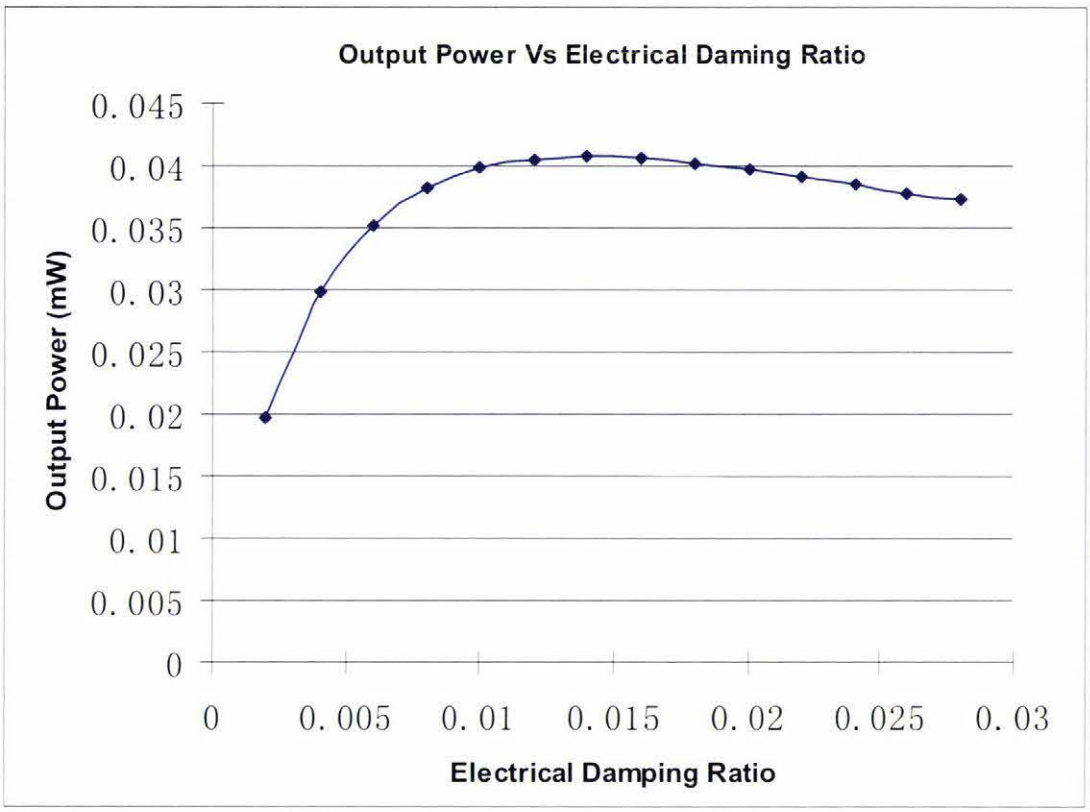


**Figure 3-9 Output power versus electrical damping ratio**

It is clear that the output power is inversely proportional to the input driving vibration frequency. The output power is optimized when the driving frequency is equal to the fundamental resonant frequency. The natural frequency of the cantilever beam can be figured out by the proof mass and the length of the beam. Therefore, the selection of the resonant frequency should match the frequency of the ambient environment source. Figure 3-10 shows the simulated power output for vs. the input driving vibration frequency.

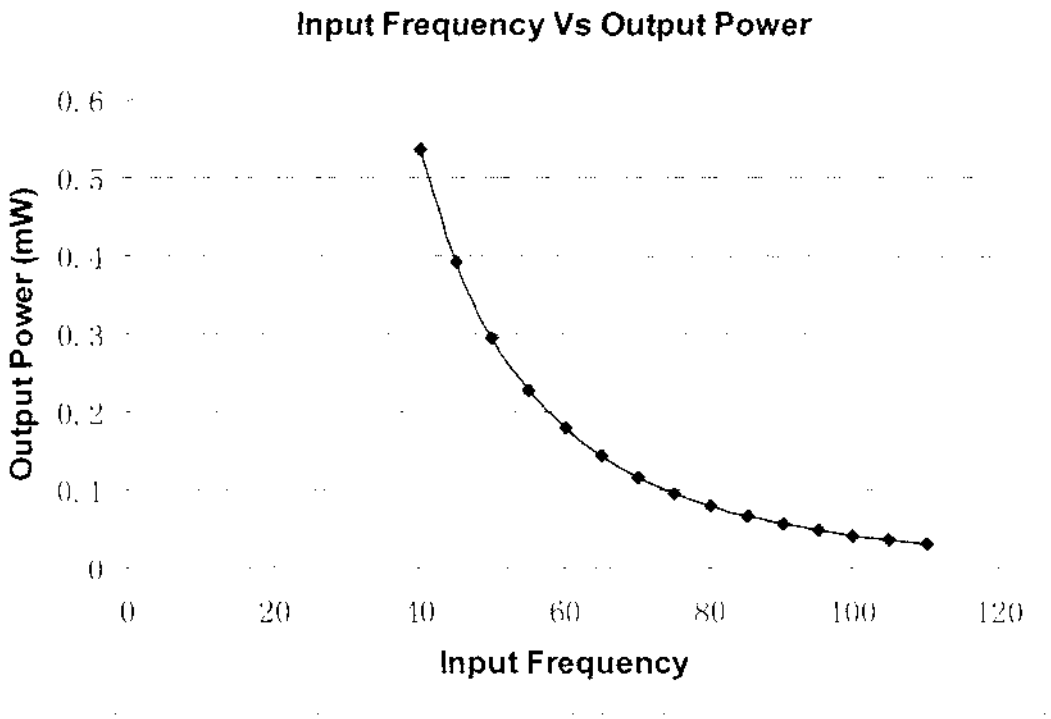


**Figure 3-10 Output power versus input frequency**

The load resistance R is the function of the equivalent electrically induced damping ratio Eq. (3.29). The proper selection of the load resistance results in optimizing the output power while $\zeta_e$ and $\zeta_m$ are equal. Figure 3-11 shows that the maximum value of the output power is around 40.8μW when the load resistance is 606 kΩ. Also it should be noted that the electrically induced damping ratio matched the mechanical damping ratio at that point.

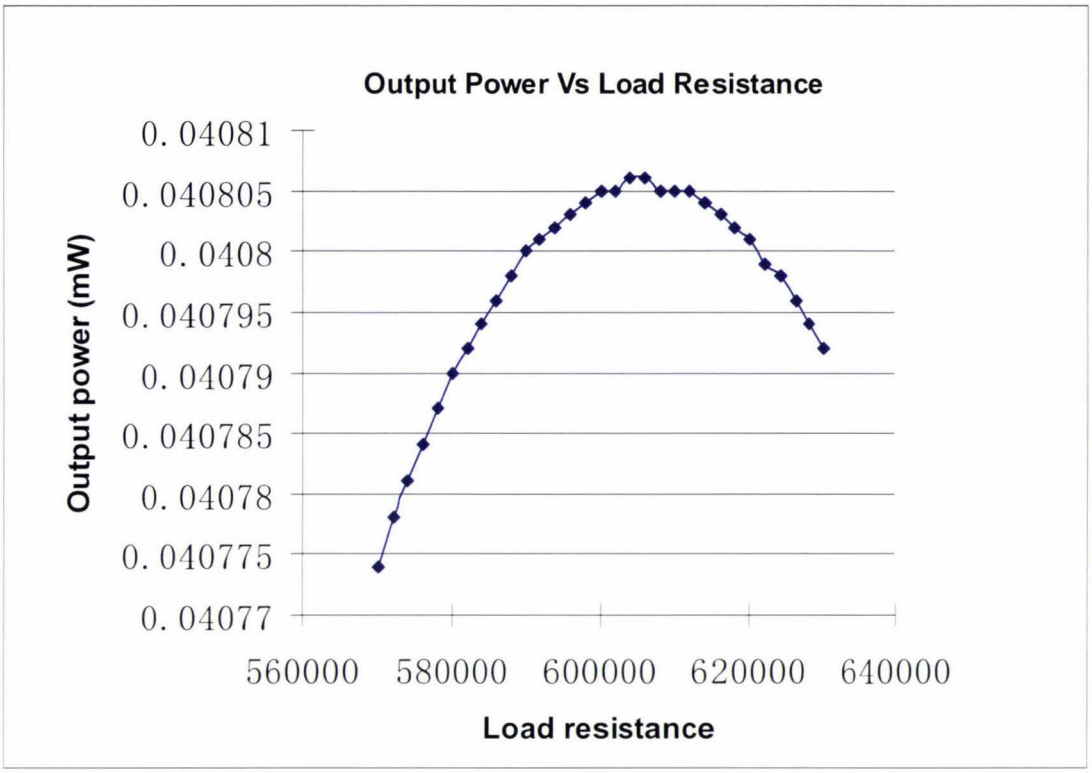


**Figure 3-11 Output power versus load resistance**

### 3.7. Conclusion

A piezoelectric bender has been chosen as the basic device due to the high stiffness of piezoelectric materials and the low frequency of most potential vibration sources. Lead zirconate titanate (PZT) is the most commonly used piezoelectric ceramic and has very good properties. Compared to the d33 mode operation the d31 mode operation is chosen for the material is chosen because of the higher strain and lower resonant frequencies.

The work presented has been focused on modeling of the PZT materials in a cantilever beam structure and discussion. Also certain functional relationships are simulated graphically. From the equation and figures the relationships are summarized as below.

- The power output is proportional to the square of the acceleration magnitude of the driving vibrations.
- Power is proportional to the proof mass of the converter, which means that scaling down the size of the converter drastically reduces potential for power conversion.
- The equivalent electrically induced damping ratio is designable, and the power output is optimized when it is equal to the mechanical damping ratio.
- For a given acceleration input, power output is inversely proportional to the input frequency.
- It is critical that the natural frequency of the conversion device closely matches the fundamental vibration frequency of the driving vibrations.

Next chapter will utilize the models and principles already developed to explore the design of a converter for monitoring traffic. It will present a case study which wireless sensor nodes are embed inside the road in order to send real time data to the access point on the side of the road.

# 4. Case Study: Power generator for use in wireless traffic monitoring sensors

## 4.1. Introduction

Increasing congestion level in public road networks is a growing problem in many countries. The 2003 Urban Mobility Report [25] estimates total annual cost of congestion for the 75 U.S. urban areas at 69.5 billion dollars, the value of 3.5 billion hours of delay and 5.7 billion gallons of excess fuel consumed.

Traffic management systems rely heavily on real-time traffic data to work efficiently to reduce traffic congestion and increase traffic efficiency. Real-time traffic data is measured and collected by traffic surveillance systems. Currently there are two main categories of traffic surveillance technologies: intrusive and non-intrusive [26]. Intrusive surveillance technologies, such as inductive loops, disrupt traffic during installation and maintenance. Non-intrusive technologies, such as video and radar detector systems, do not disrupt traffic and they are highly flexible. Nevertheless, the accuracy of these systems varies significantly with environmental conditions. Furthermore the cost of equipment of these systems is usually very high. Recently, wireless magnetic sensor networks have been proposed as a very attractive alternative to existing technologies for traffic surveillance in terms of cost, ease of deployment and maintenance, and enhanced measurement capabilities [27].

Wireless magnetic sensor networks offer a very attractive alternative to inductive loops for traffic surveillance on freeways and at intersections in terms of cost, ease of deployment and maintenance, and enhanced measurement capabilities. Coleri et al [28] has built a prototype of the sensor node for traffic surveillance, which was called Traffic-Dot. These networks consist of a set of sensor nodes (SN) and one access point (AP). A SN comprises a magnetic sensor, a microprocessor, a radio, and a battery. Each SN is encased in a 5"-diameter 'smart stud' container that can be glued to the centre of a lane for temporary deployment or embedded into the ground for permanent installation. The SNs detect vehicles by measuring the change in the Earth's magnetic field, and send their data via radio to the AP on the side of the road.

The AP forwards received data to the traffic management system via GPRS or to the roadside controller. Two SNs placed a few meters apart can estimate speed.

The processor and the radio are located in MICA2DOT, the latest family of Berkeley motes [29]. The microprocessor is Atmel ATmega128L with 128kB of programmable memory and 512kB of data flash memory. It runs TinyOS, an operating system developed at UC Berkeley, from its internal flash memory. TinyOS enables the single processor board to run the sensor processing and the radio communication simultaneously.

The radio is ChipCon CC1000 916MHz, frequency shift keying (FSK) RF transceiver, capable of delivering up to 40 Kbps. The RF transmit power can be changed in software. There are two HMC1051Z magnetic sensors, based on anisotropic magnetoresistive (AMR) sensor technology. To receive one sample, the magnetometer is active for 0.9 msec and the energy spent for taking one sample is 0.9μJ. The magnetometer is turned off between samples for energy conservation [28].

**Figure 4-1 Sensor node [27]**

The battery shown in Figure 4-2 is Tadiran Lithium TL5135, with 1.7Ah capacity, diameter in 1.29 inch (3.28cm) and height in 0.41 inch (1.0414cm). The entire unit is encased in a SmartStud cover, designed to be placed on pavement and able to withstand 16,000 Lbs. So the node is protected and can be glued on anywhere on the pavement.


**Figure 4-2 TL5135 battery [30]**

The power-consuming operations in a sensor node are transmission and reception of a packet, listening to the channel, sampling, and running the microprocessor. The researchers [27] point out that if each sensor node has a pair of AA batteries, which can supply 2200 mAh at 3 V, the lifetime of sensor node system is about 1200days. Therefore, the average energy consumption per day is 2.2 Ah * 3 V / 1200 *3600 Sec= 19.8 J/day. In Chapter 4, the power consumption is considered as the reference for generator design.

However, the proposed wireless sensor networks use batteries to power each SN. As a battery only lasts for about three years, it would be a huge job to change the underground batteries if wireless sensor networks are widely deployed. An alternative to batteries is to make use of ambient energy that is available in the surrounding environment. A device that scavenges energy efficiently from the environment is called an energy scavenger. Integration of energy scavengers and devices leads to energy self-sufficient devices where there is no need to replace their depleted power supplies. Energy scavenging has been drawing a lot of interests from both research and industry as the demand for alternative and clean energy escalates in recent years [31].

According to the initial study, cantilever beam has advantages including relatively low resonance frequency and high average strain for a given input force [32], making it suitable for harvesting energy from the traffic environment. Given appropriate power conditioning and capacitive storage, the resulting power source should be sufficient to support networks of ultra-low-power, peer-to-peer traffic surveillance wireless nodes.

When cars pass cantilever-based devices with PZT encased in the sensor node, it can produce vibrations with frequencies predominantly in the range from 5 to 25 Hz. The amplitude of the vibrations ranges between 0.005 and 2 $m/s^2$ (0.0005 and 0.2 g) measured as acceleration [33]. The predominant frequencies and amplitude of the vibration are changed due to many factors including the condition of the road; vehicle weight, speed and suspension system; soil type and stratification; season of the year etc. The effects of these factors are interdependent and it is difficult to specify simple relationships between them.

The report is assumed that the device will replace the battery and the sensor node is placed in a busy road or freeway with vibrations at 25 Hz with an acceleration magnitude of 0.05 $m/s^2$. Therefore, the total volume of the prototype piezoelectric generator is approximately 3.28cm*3.28cm*1.04cm = 11.2 $cm^3$. The prototype was then driven with vibrations of 0.05 $m/s^2$ at 25 Hz. Vibrations drive the device, the generator provides an AC voltage. Therefore, it is assumed that the converter is driven with vibrations at 25 Hz with an acceleration magnitude of 0.05 $m/s^2$ in this case. The mathematical models developed are implemented in Matlab (v7.1) with optimization function using the Sequential Quadratic Programming (SQP). The optimization details have been given and models developed for this application are then compared with the experimental results.

In addition it is also possible to scavenge power by applying a force from the weight of a car. In section 4.3 the comparison of cantilever mounted bending mode and cantilever beam vibration mode will be made.

### 4.2. SQP implementation

This optimization of the application was implemented in Matlab (7.0) with its built in functions that use a Sequential Quadratic Programming (SQP) method. There are three primary stages in the SQP implementation. They are discussed briefly in the following subsections:

- Updating of the Hessian matrix of the Lagrangian function
- Quadratic programming (QP) problem solution

- Line search and merit function calculation

### *4.2.1. Updating the Hessian matrix*

In each iteration, a positive definite quasi-Newton approximation of the Hessian of the Lagrangian function, H, is calculated using the Broyden-Fletcher-Goldfarb-Shano (BFGS) method, where λi (i = 1,..,m) is an estimate of the Lagrange multipliers.

$$H_{k+1} = H_k + \frac{q_k q_k^T}{q_k^T s_k} - \frac{H_k^T H_k}{s_k^T H_k s_k} \tag{4.1}$$

where

$$s_k = x_{k+1} - x_k$$

$$q_k = \nabla f(x_{k+1}) + \sum_{i=1}^{n} \lambda_i \cdot \nabla g_i(x_{k+1}) - \left\{ \nabla f(x_k) + \sum_{i=1}^{n} \lambda_i \cdot \nabla g_i(x_k) \right\}$$

Powell 0 suggests the Hessian matrix is positive definite even though it might be positive indefinite at the solution point. The function $q_k^T s_k$ needs to be positive at each update in a positive definite Hessian and that H is initialized with a positive definite matrix. When $q_k^T s_k$ is negative, $q_k$ is modified on an element-by-element basis to keep $q_k^T s_k > 0$. This procedure is continued until $q_k^T s_k$ is greater than or equal to 1e-5. If, after this procedure, $q_k^T s_k$ is still not positive, modify $q_k$ by adding a vector v multiplied by a constant scalar w, that is,

$$q_k = q_k + wv \tag{4.2}$$

where

$v_i = \nabla g_i(x_{k+1}) \cdot g_i(x_{k+1}) - \nabla g_i(x_k) \cdot g_i(x_k)$,

if

$(q_k)_i \cdot w < 0$ and

$(q_k)_i \cdot (s_k)_i < 0 (i = 1,...m)$

$v_i = 0$ otherwise increase w systematically until $q_k^T s_k$ becomes positive.

If the Hessian matrix is kept positive definite using the first phase of the previous procedure, then Hessian modified is shown. If QP problem is not feasible, then infeasible is displayed. If the message no update is displayed, that means $q_k^T s_k$ is nearly zero.

### *4.2.2. Quadratic programming solution*

Each QP problem can be solved at a main iteration of the SQP method, where $A_i$ refers to the i[th] row of the m-by-n matrix $A$. The form is shown below.

$$\underset{d \in \Re^n}{\textbf{minimize}} \quad q(d) = \frac{1}{2} d^T H d + c^T d \qquad (4.3)$$

$$A_i d = b_i \qquad i = 1,\ldots,m_e$$
$$A_i d \le b_i \qquad i = m_e + 1,\ldots,m$$

This form is as alike as that of Gill et al., described in [35] and [36] and implemented in the Optimization Toolbox. It has been adjusted for both QP problems and Linear Programming (LP).

The solution procedure involves two phases. The first phase is to calculate a feasible point (if one exists). The second phase is to generate an iterative sequence of feasible points for converging to the solution. In this way the active constraints at the solution point is evaluated by keeping an active set $\overline{A}_k$ (i.e., those that are on the constraint boundaries). Actually all QP algorithms are active set methods. These methods are emphasized because a lot of different methods have a similar in structures but that are described in widely different terms.

A basis $\overline{A}_k$ gives a solution for each search direction by being updated at each iteration k. Equality constraints are maintained in the active set $\overline{A}_k$. The variable $\hat{d}_k$ used here is distinguished it from $d_k$ in the major iterations of the SQP method. The calculation of each search direction $\hat{d}_k$ is solved under the constraint boundaries and it can minimize the objective function. The columns of a basic $Z_k$ are vertical to the estimate of the active set $\overline{A}_k$ (i.e., $\overline{A}_k Z_k = 0$) and form the feasible subspace for $\hat{d}_k$.

Therefore, a search direction is calculated by summarizing linearly any combination of the columns of $Z_k$, is guaranteed to remain on the boundaries of the active constraints.

The matrix $Z_k$ is formed from the last $m-l$ columns of the QR decomposition of the matrix $\overline{A}_k^T$, where l is the number of active constraints and l < m. That is, $Z_k$ is given by:

$$Z_k = Q[:, l+1:m] \tag{4.4}$$

where

$$Q^T \overline{A}_k^T = \begin{bmatrix} R \\ 0 \end{bmatrix}$$

If $Z_k$ is obtained, then a new search direction $\hat{d}_k$ is to be set to minimize $q(d)$ where $\hat{d}_k$ is in the null space of the constraints boundary. That is, $\hat{d}_k$ is a linear combination of the columns of $Z_k$ : $\hat{d}_k = Z_k p$ for some vector p.

Then if the quadratic is treated as a function of p, by substituting for $\hat{d}_k$, then it will have

$$q(p) = \frac{1}{2} p^T Z_k^T H Z_k p + c^T Z_k p \tag{4.5}$$

Differentiating this with respect to p yields

$$\nabla q(p) = Z_k^T H Z_k p + Z_k^T c \tag{4.6}$$

$\nabla q(p)$ is defined by $Z_k$ in the subspace and it is treated as the projected gradient of the quadratic function. The term $Z_k^T H Z_k$ is called the projected Hessian. If the Hessian matrix H is implemented in SQP method and positive definite, so the function q(p) in the subspace is minimum, which is defined by $Z_k$ occurs when $\nabla q(p) = 0$, which is the solution of the system of linear equations:

$$Z_k^T H Z_k p = -Z_k^T c \tag{4.7}$$

A step is then taken of the form

$$x_{k+1} = x_k + \alpha \hat{d}_k \qquad \text{where } \hat{d}_k = Z_k^T p \tag{4.8}$$

There are only two options of step size α., at each iteration because of the quadratic nature of the objective function. Each step of a whole along $\hat{d}_k$ is the exact step to the minimum of the function restricted to the null space of $\overline{A}_k$. If such a step can be obtained under the constraints, then this is the solution to QP (Equation 4.4). In addition, a new constraint is involved in the active set at the next iteration assuming the step size to the closest restriction is less than unity. The distance to the restriction boundaries in any direction $\hat{d}_k$ is given by:

$$\alpha = \begin{matrix} i \\ \end{matrix} \left\{ \frac{-(A_i x_k - b_i)}{A_i \hat{d}_k} \right\} \qquad (i = 1,\ldots,m) \tag{4.9}$$

which is described as restrictions not in the active set, and where the direction $\hat{d}_k$ is towards the restriction boundary, i.e., $A_i \hat{d}_k > 0, i = 1,\ldots,m$.

When n independent restrictions are included in the active set, without location of the minimum, Lagrange multipliers, $\lambda_k$, are calculated that satisfy the non-singular set of linear equations:

$$\overline{A}_k^T \lambda_k = c \tag{4.10}$$

If all elements of $\lambda_k$ are positive, $x_k$ is the optimal solution of QP (Equation 4.4). Nevertheless, if any element of $\lambda_k$ is negative and the element does not accord with an equality constraint, then the corresponding element is deleted from the active set and a new iterate is sought.

The algorithm needs a feasible starting point. If the given starting point from the SQP method is unfeasible, then a point can be obtained by solving the linear programming problem:

(4.11)

$$\begin{aligned} &\underset{\gamma \in \Re, x \in \Re^n}{\textbf{minimize}} \quad \gamma \\ &A_i x = b_i \qquad i = 1,\ldots,m_e \\ &A_i x - \gamma \le b_i \qquad i = m_e + 1,\ldots,m \end{aligned}$$

The notation $A_i$ indicates the $i^{th}$ row of the matrix $A$. A feasible point (if one exists) to Equation 4.11 can be found by setting x to a value that satisfies the equality constraints. This value is easily obtained by working out an under- or over determined group of linear equations consisted of the group of equality constraints. Once this problem gets a solution, then the slack variable $\gamma$ is defined to the maximum inequality constraint at this point.

However, the previous QP solution for LP problems can be changed by defining the search direction to the steepest decline direction at each iteration, where $g_k$ is the gradient of the objective function which is equal to the coefficients of the linear objective function.

$$\bar{d}_k = -Z_k Z_k^T g_k \tag{4.12}$$

When a feasible starting point is determined using the previous LP solutions, the primary QP phase is introduced. The first search direction $\hat{d}_1$ of $\hat{d}_k$ can be found by solving the set of linear equations:

$$H\hat{d}_1 = -g_k \tag{4.13}$$

where $g_k$ is the gradient of the objective function at the current iteration $x_k$, for example: $Hx_k + c$.

However, when a feasible point is not discovered for the QP problem, the direction of search for the main SQP routine $\hat{d}_k$ is treated as one that minimizes $\gamma$.

### *4.2.3. Line search and merit function*

For each iteration of the QP subproblem the direction $d_k$ is calculated by below equation:

$$x_{k+1} = x_k + \alpha d_k \tag{4.14}$$

In order to create a sufficient decrease in a merit function the step size parameter $\alpha_k$ need to be defined. Han [36] and Powell 0 implement the merit function in the following equation:

$$\psi(x) = f(x) + \sum_{i=1}^{m_e} r_i \cdot g_i(x) + i = \sum_{i=m_e+1}^{m} r_i \cdot \max\{0, g_i(x)\} \tag{4.15}$$

Powell suggests setting the compensation parameter:

$$r_i = (r_{k-1})_i = \max_i \left\{ \lambda_i, \frac{1}{2}((r_k)_i + \lambda_i) \right\}, \qquad i = 1, \ldots, m \tag{4.16}$$

The compensation parameters result in positive contribution from the inactive constraints in the QP solution but were recently active. In this performance, the compensation parameter $r_i$ is initially set to

$$r_i = \frac{|\nabla f(x)|}{|\nabla g_i(x)|} \tag{4.17}$$

where $|\ |$ represents the Euclidean norm.

The implementation assures larger contributions to the compensation parameter from constraints with smaller gradients, which would be the case for active constraints at the solution point.

## 4.3. Design optimization

### *4.3.1. Cantilever beam vibration mode*

A cantilever beam with piezoelectric material has been chosen as the power generator scavenging energy from the potential vibration sources. The bender operates in 31 mode and this kind of bimorph structure benefits lower stiffness and higher strains which can be generated with a given force input. Also PZT material has been chosen as the primary material in the design and analysis.

Once the prototype of the piezoelectric converter is defined and simulated, the design model can be optimized by mathematical tools. A regular mathematical optimization can be implemented in order to choose dimensions and design parameters. The variables over which the design can be optimized are shown in Table 3-3.

The relationship between mass and power output is proportional. A higher dense material for the proof mass is better to a less dense material due to the fact that the designs will generally be constrained by volume, not weight. Tungsten is the densest commonly used material with density of 19g/cm$^3$. Other more dense materials are not commonly available but radioactive. In the following the designs of using two masses are compared. One mass is tungsten alloy metal with 17 g/cm$^3$, another is a mass of tool steel with 7.715 g/cm$^3$. They are assumed as the material for the proof of 0.05 m/s$^2$ at 25 Hz. The mechanical damping ratio for these two simulations was 0.02.

The optimization problem can be formulated as follow:

*Maximize* $P = f(l_m, h_m, w_m, l_b, w_b, l_e, t_p, t_{sh}, R_{load})$

*Subject to*

$$(l_b + l_m)\, w_m\, h_m <= 11.2\ cm^3$$

$$(l_b + l_m)\, w_b\, h_m <= 11.2\ cm^3$$

$$F = 25\ Hz$$

$$l_e - l_b - l_m <= 0$$

$$l_m, h_m, w_m, l_b, w_b, l_e, t_p, t_{sh}, R_{load} >= 0$$

The linear constraint, $l_e - l_b - l_m <= 0$, results from the fact that it is physically impossible for the electrode length to be longer than the sum of the beam and mass lengths. The equation constraints the driven frequency, F = 25 Hz is a constraint, and the frequency is an implication of design parameters. The first two non-linear constraints, $(l_b + l_m)\ w_m\ h_m <= 11.2\ cm^3$ and $(l_b + l_m)\ w_b\ h_m <= 11.2\ cm^3$, represent overall volume constraints, because the goal in the design was to build a vibration converter that fits a space of $11.2cm^3$ or less. Finally, the maximum strain cannot exceed the yield strain of the piezoelectric material, which leads to the third non-linear constraint. Although strain is not a direct function of the design parameters, it can be used as a non-linear optimization constraint.

The optimization problem can be solved using the Sequential Quadratic Programming (SQP) method (available in Matlab). In this method, the nonlinear optimization problem is converted to a quadratic programming (QP) subproblem at each iteration. As mentioned in Chapter 4.2 the SQP implements the optimization algorithm to find for the optimal values of the variables. The problem consists of four subroutines: the object subroutine that defines known constants and output power function; the constraint subroutine that sets the linear and non-linear constraints; the running subroutine, the main program that performs global optimization starting from selected initial values of the variables.

The selection of the initial values of the variables is the important issue affecting the final optimal result because the nonlinear problem often has lots of local minima. In order to find the global optimum result, trying and running as many suitable starting points as possible is necessary. In this study a program was developed to calculate all possible starting points for the optimization under its function and constraints.

For the Tungsten alloy metal, there are 94 starting points that satisfies the optimization constraint and 94 global optimal powers are found and stored in an array, from which the best design can be easily found and the optimal variables that describe the cantilever in Table 4-1 are obtained.

**Table 4-1 Variables description**

| Variables | Description |
|---|---|
| $l_m$ | Length of the mass |
| $h_m$ | Height of the mass |
| $w_m$ | Width of the mass |
| $l_b$ | Length of the cantilever beam |
| $w_b$ | Width of the cantilever beam |

The below figures (Figure 4-1 to 4-6) present the power variation over the optimising procedure, computed by fmincon function, at the various initial points. Figure 4-1 and 4-2 show the nearly same final optimal value around 0.0017W while the result shown in Figure 4-3 is not as good as the above.

Summarised in Table 4-2 are the criteria with which the optimization iteration in terminated.

**Table 4-2 Symbol interpretation**

| Symbol | Interpretation |
|---|---|
| 1 | First order optimality conditions were satisfied to the specified tolerance. |
| 2 | Change in x was less than the specified tolerance |
| 3 | Change in the objective function value was less than the specified tolerance |
| 4 | Magnitude of the search direction was less than the specified tolerance and constraint violation was less than options.TolCon |
| 5 | Magnitude of directional derivative was less than the specified tolerance and constraint violation was less than options.TolCon. |

The default values of options.TolCOn, options.TolFun and options.TolX are 1e-6, where TolCon, TolFun, TolX represents termination tolerance on the constraint violation, termination tolerance on the function value and termination tolerance on x, respectively.

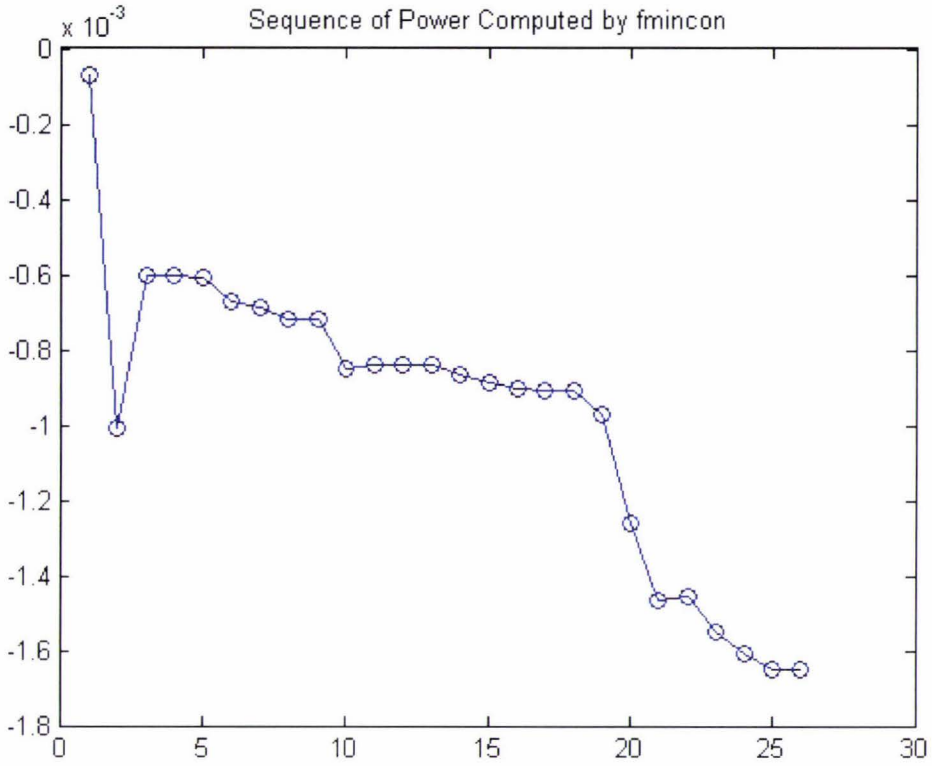


**Figure 4-1 Optimising procedure of first starting point with Tungsten alloy metal**

In Figure 4-1, the algorithm is terminated in criterion 1, 2, 4 and 5 after running 26 iterations. The result is the optimal power of 1.7mW and the variables of are $l_m$ = 31.9mm, $h_m$ = 10mm, $w_m$ = 10mm, $l_b$ = 10mm and $w_b$ = 25.2mm

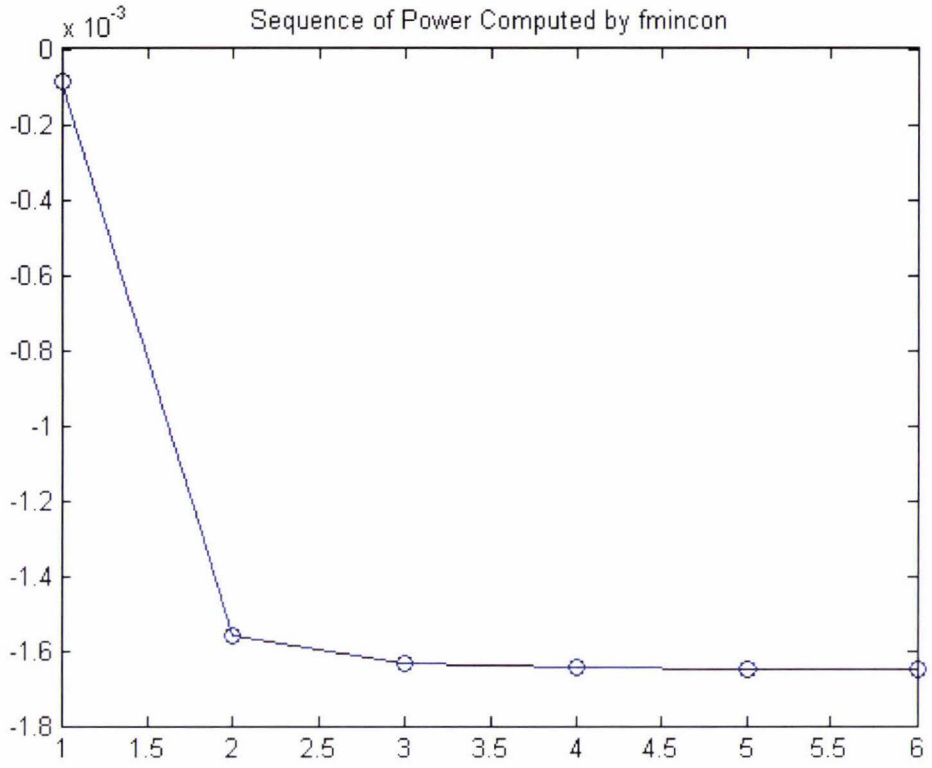


**Figure 4-2 Optimising procedure of second starting point with Tungsten alloy metal**

In Figure 4-2, it is obvious that there are 6 iterations when the program is terminated. According to the termination report, the optimization was finished due to criterion 1, 2, 4 and 5 while the optimal results are same as before.

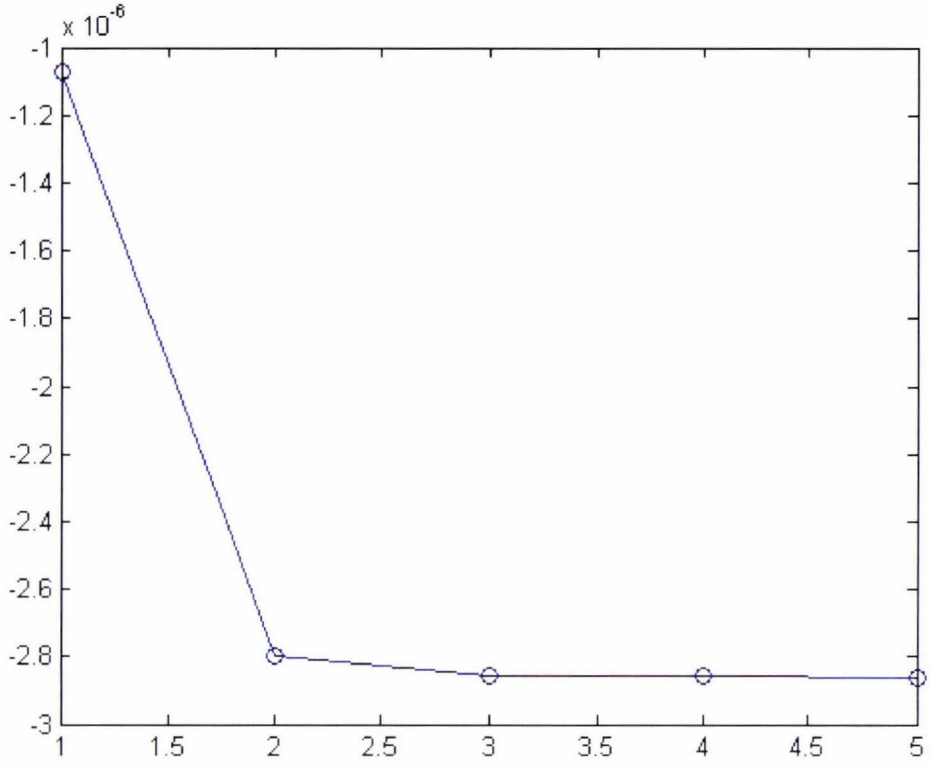


**Figure 4-3 Optimising procedure of third starting point with Tungsten alloy metal**

In Figure 4-3, the search for optimization is terminated by criterion 2, 4 and 5 after running 5 iterations. According to the termination report, the magnitude of search direction less than 2*options.TolX and maximum constraint violation is less than options.TolCon. The optimal power is very low, only 2.9e-3mW and the value of the optimal variables are $l_m$ = 10.1mm, $h_m$ = 44.6mm, $w_m$ = 10mm, $l_b$ = 10mm and $w_b$ = 18.4mm.

For the mass of tool steel with 7.715 g/cm$^3$, after running a search program, 94 starting points were found that match the optimization requirement and 94 optimal designs were found and saved in an array. The results are explained briefly below.

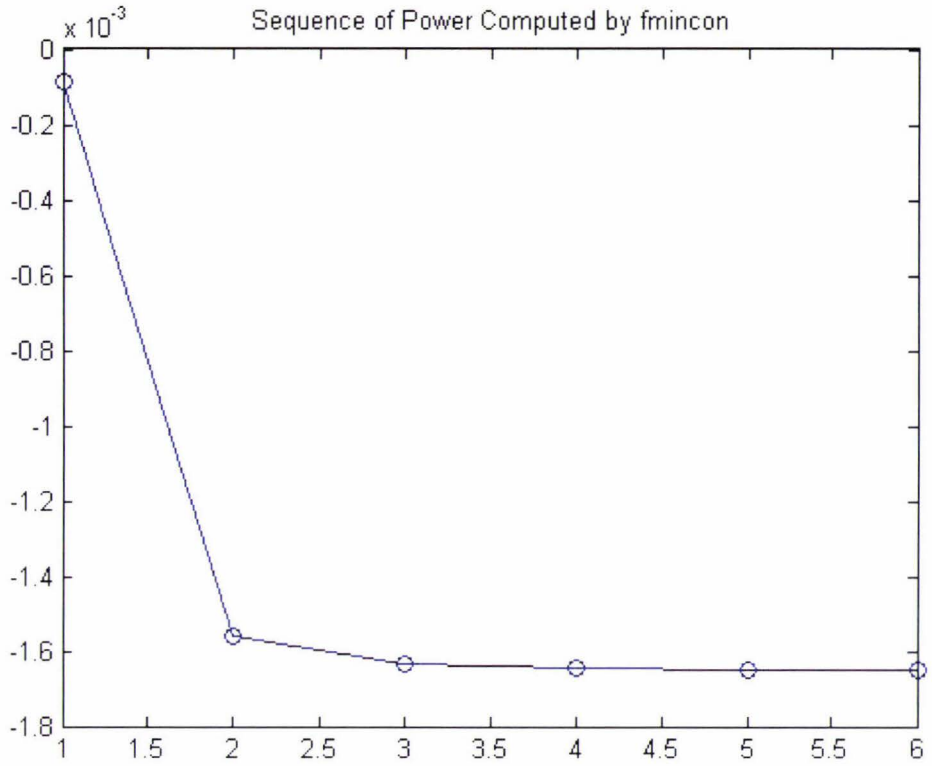


**Figure 4-4 Optimising procedure of first starting point with tool steel**

In Figure 4-4, the algorithm was terminated by criterion 1, 2, 4 and 5. The termination report states: first-order optimality measure less than options.TolFun and maximum constraint violation is less than options.TolCon. The optimal result is: the optimal power of 1.7mW and the values of the optimal variables $l_m$ = 38.5mm, $h_m$ = 10mm, $w_m$ = 10mm, $l_b$ = 10mm and $w_b$ = 21.7mm.

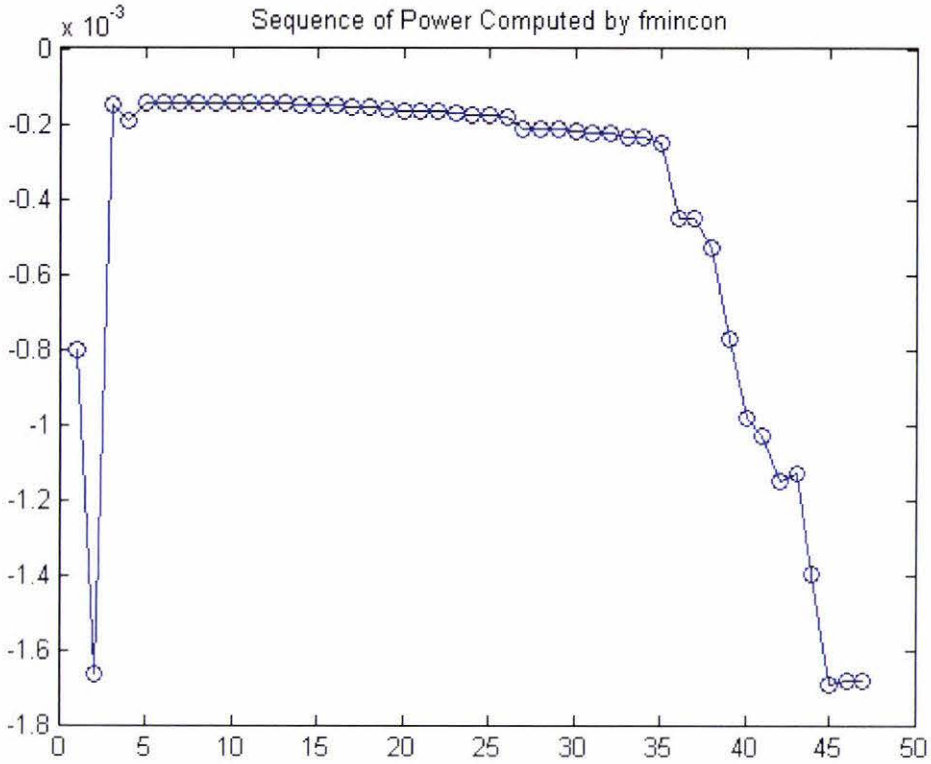


**Figure 4-5 Optimising procedure of second starting point with tool steel**

The iteration was terminated by criterion 1, 2, 4 and 5 while first-order optimality measure less than options.TolFun and maximum constraint violation is less than options.TolCon. The optimal results are same as those in Figure 4-4.

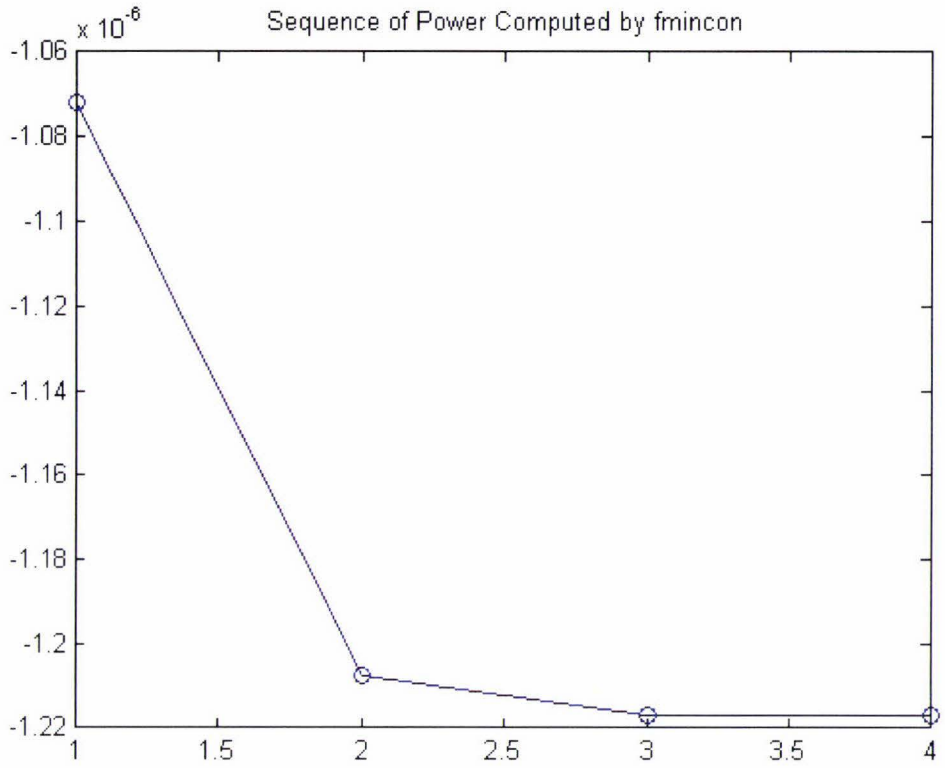


**Figure 4-6 Optimising procedure of third starting point with tool steel**

The iteration was terminated by criterion 4 and 5. The termination report states that magnitude of search direction less than 2*options.TolX and maximum constraint violation is less than options.TolCon. It's the worst starting point with which poorest optimal results were obtained.

In summary, each result of the starting point represents a local optimal point. The optimum value may occur in a lot of local optimal points. Two starting points may have two big different optimal values according to Figure 4-1 and Figure 4-3, Figure 4-4 and Figure 4-6. Therefore, finding a right starting point is a very import factor to get the global optimum value in this program. Two materials have been compared and optimized in Matlab. On the other hand the higher dense material, tungsten alloy metal, was not available in the workshop and the tool steel was used instead in this study. Several starting points out of 94 are suitable for the constraints. Table 4-3 shows the best optimized design.

**Table 4-3 Optimal design parameters**

| Variables | Description | Optimized Value | Range Allowed |
|---|---|---|---|
| $l_m$ | Length of the mass | 38.5mm | $l_b + l_m$ <=62.4mm, size of PZT |
| $h_m$ | Height of the mass | 10mm | $h_m$ <=10mm |
| $w_m$ | Width of the mass | 10mm | wm<=10mm |
| $l_b$ | Length of the cantilever beam | 10mm | $l_b + l_m$ <=62.4mm, size of PZT |
| $w_b$ | Width of the cantilever baem | 21.7mm | $w_b$<=10mm |
| $l_e$ | Length of the electrode on the beam surface | 10mm | All,subject total volume constraint |
| $t_p$ | Thickness of one piezoelectric layer | 0.267mm | $t_p$ = 0.267mm |
| $t_{sh}$ | Thickness of the center shim | 0.102mm | $t_{sh}$ = 0.102mm |
| $R_L$ | Load resistance | 247.5KΩ | All greater than zero |
| P | Output power | 1.7mW | |

Therefore, according to above specified dimensions, the final prototype was designed in Solidwork (Figure 4-7).

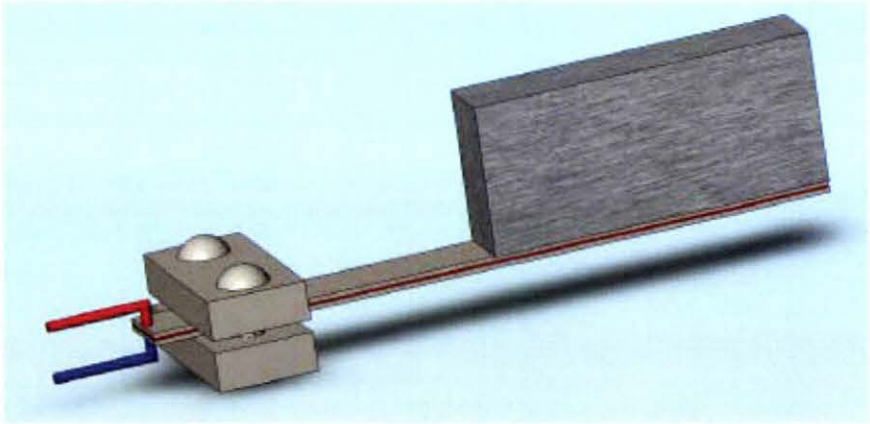

**Figure 4-7 Modelling of cantilever beam**

### *4.3.2. Bending mode*

When a mechanical force causes a suitably polarized 2-layer element to bend, one layer is compressed and the other is stretched. Charge develops across each layer in an effort to counteract the imposed strains. This charge may be collected. It's assumed that cars pass and apply a force at the free end of the cantilever which is buried under the road in advance. Therefore, under the assumption that the strain is distributed evenly along the bender, let's consider a cantilever mounted bender with width W, length L, thick t, charge coefficient d31, voltage coefficient g31, Young's modulus Y, and maximum surface strain $S_{max.}$ as shown in Figure 4-8.

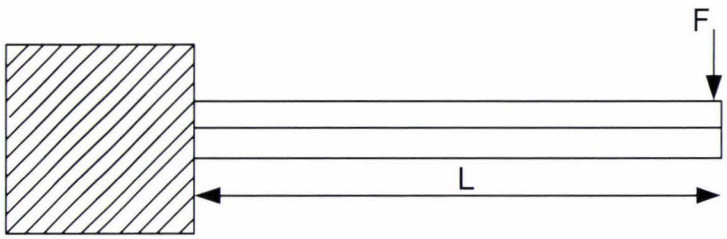


**Figure 4-8 Bending mode**

By applying a force, F, at the free end, the voltage across the thickness direction is shown below [37].

$$V = \frac{3FLg_{31}}{2Wt} \tag{4.18}$$

So, the total available energy per bending is

$$E = \frac{1}{2}CV^2 = \frac{1}{2}\frac{\varepsilon LW}{t_c}\frac{9F^2L^2g_{31}^2}{4W^2t_c^2} = \frac{9\varepsilon L^3F^2g_{31}^2}{8t_c^3w} \tag{4.19}$$

Note that $F = k_s\Delta x$, where $\Delta x$ is the free end deflection and $k_s$ is the equivalent stiffness of the bender as below.

$$k_s = \frac{3YI}{L^3} \tag{4.20}$$

where $I$ is inertia moment expressed in equation 3.7. Substituting equation 3.7 into 4.20, then the stiffness of the bender can be solved in following expression:

$$k_s = \frac{6Y}{L^3}\left(\frac{wt_c^3}{12} + wt_c b^2\right) + \frac{Y^2 wt_{sh}^3}{4Y_{sh}L^3} \tag{4.21}$$

Substituting equation (4.21) into (4.19), the energy in terms of bender's physical dimensions is shown below.

$$E = \frac{9\varepsilon g_{31}^2}{8t_c^3 wL^3}\cdot\left[6Y\left(\frac{wt_c^3}{12} + wt_c b^2\right) + \frac{Y^2 wt_{sh}^3}{4Y_{sh}}\right]^2 \cdot \Delta x^2 \tag{4.22}$$

Note that the surface strain $S_{\max} = \frac{t_c \Delta x}{L^2}$, constrain the maximum energy value with $S_{max}$ as below.

$$E_{\max} = \frac{9\varepsilon g_{31}^2 LwY^2}{8t_c}\cdot\left[6\left(\frac{t_c^3}{12} + t_c b^2\right) + \frac{Yt_{sh}^3}{4Y_{sh}}\right]^2 \cdot S_{\max} \tag{4.23}$$

The maximum surface stain of the PZT is approximately 500 microstrain (micrometers per meter) [PZT], which is constrained by the limited device size. $\varepsilon, Y, Y_{sh}, g_{31}$ are constants determined by the material properties. Therefore, the expression was simple to be solved by using optimization toolkit in Matlab. After optimization the maximum available power is 0.68mW generated in bending mode. The maximum tolerance of deflection is 0.004m, which constrains the force F on the free end to move up or down range in 4mm, otherwise the bender may be broken. If the bending mode device is used in this case, it will only accept 4mm distortion in vertical direction whatever the car weight is.

### *4.3.3. Mounted bender mode*

In mounted bender mode a thickness direction force F at the middle of the bender, is shown in Figure 4-9.

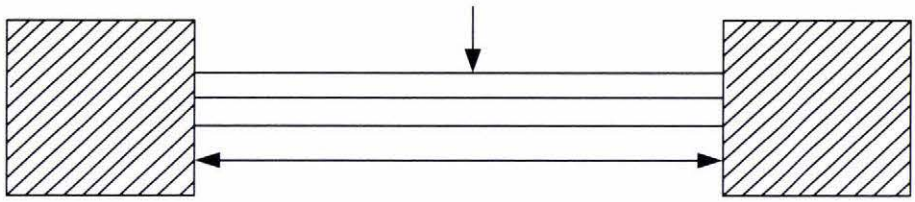

**Figure 4-9 A mounted bender**

According to [23], the voltage across the thickness direction is shown below.

$$V' = \frac{1}{4} \cdot \frac{3FLg_{31}}{2wt} \tag{4.24}$$

Going through a similar procedure as above, the available energy is shown below.

$$E' = \frac{9\varepsilon g_{31}^2 Y^2 w}{128 t_c^3 L^3} \cdot \left[ 6\left( \frac{t_c^3}{12} + t_c b^2 \right) + \frac{Y t_{sh}^3}{4 Y_{sh}} \right]^2 \cdot \Delta x^2 \tag{4.25}$$

Note that the surface strain $S_{\max} = \frac{4 t_c \Delta x}{L^2}$, constrain the maximum energy value with $S_{max}$ as below.

$$E_{\max}{}' = \frac{9\varepsilon g_{31}^2 L w Y^2}{8 t_c} \cdot \left[ 6\left( \frac{t_c^3}{12} + t_c b^2 \right) + \frac{Y t_{sh}^3}{4 Y_{sh}} \right]^2 \cdot S_{\max} \tag{4.26}$$

The energy equation is the same as the bending mode. Therefore the available energy of mounted bender mode is 0.68mW as well. And the maximum surface strain is 0.001m, which has lower movement tolerance than the mounted bender mode. However, in [38], researchers considered that for a mounted bender, if the bender is originally flattened, it is difficult to make a deflection when it is attached to the heel. A better way to do it is to use the preloaded bender, which is a simple mounted device with deflection at original shape. When a force is applied to such pre-loaded devices at the opposite direction of its original deflection, the bender will be flattened. The strain change will induce a voltage across the two side of the bender. Theoretically, the absolute strain will be the same as flat bender; therefore, the induced voltage

should be the same. However, the experiment data has shown that the pre-loaded bender has much better piezoelectric properties than a flat bender, such as higher d31 coefficients [39].

### 4.4. Conclusion

Three feasible power generator modes have been modelled and optimized under volume and frequency constraints. All the power converters are assumed from a vibration source of $0.05m/s^2$ at 25 Hz and constrained in volume $0.0328m*0.0328m*0.010414m = 11.2cm^3$. The cantilever beam vibration mode is the best choice generating higher available power which has 1.7mW. Also, the generated resistive load of the optimal design is possible. Therefore, the power output value predicted for capacitive load circuit is considered useful and realistic.

In the sensor networks for monitoring traffic system, the power consumption of a sensor node is 19.8 J/day which is mentioned in Chapter 4-1. When cars pass through the road embedded piezoelectric vibration-to-electricity converters constantly, the generated energy is saved in a power storage circuit. The amount of the needed time can be calculated in equation 4-27.

$$T = \frac{19.8}{1.7\times10^{-3}} \cdot \frac{1}{60\times60} \approx 3.5 hours \qquad (4.27)$$

It presents that the embedded sensor node can be powered in a whole day if the converter device scavenges energy from ambient environment for 3.5 hours. It is possible and easy to implement it in a busy road. When the mechanical energy converts to electrical energy, there will be energy loss at any time. Therefore, the more charge time will be needed. Once the model to predict the output of piezoelectric generator is developed and optimized the piezoelectric converter will be built and tested in the experiment.

# 5. Circuit design for power storage

## 5.1. Introduction

An issue for vibration-based devices is the requirement for energy storage. Development of a self-powered sensor system requires the construction of a high efficiency power supply circuit to store the charge produced by the piezoelectric element and drive the sensor system. Power management is required to serve for microcontroller Atmel ATmega128L and transmission.

Reference [40] has shown that a PZT based preloaded bender performs high voltages output and low current output behaviour. MIT media lab has come up with the experiment data of 306 volt on shoe-mounted piezoelectric. Table 5-1 shows the energy and voltage in pre-loaded bending mode. It is easy to calculate the current output with the lower milliampere level.

**Table 5-1 Pre-loaded bending generator**

| Model | TH-6R | TH-7R | TH-8R |
|---|---|---|---|
| Voltage (V) | 670 | 560 | 230 |
| Power (mW) | 133 | 111 | 8 |

In the case study the output voltage is 230 volt, which can be obtained from the optimization program in previous Chapter. Therefore, a suitable transformer is needed before connecting the storage circuit.

In this Chapter, a circuit design is detailed and its principal is illustrated.

## 5.2. Circuit design

The fundamental circuit construction consists of six components are shown in Figure 5-1.

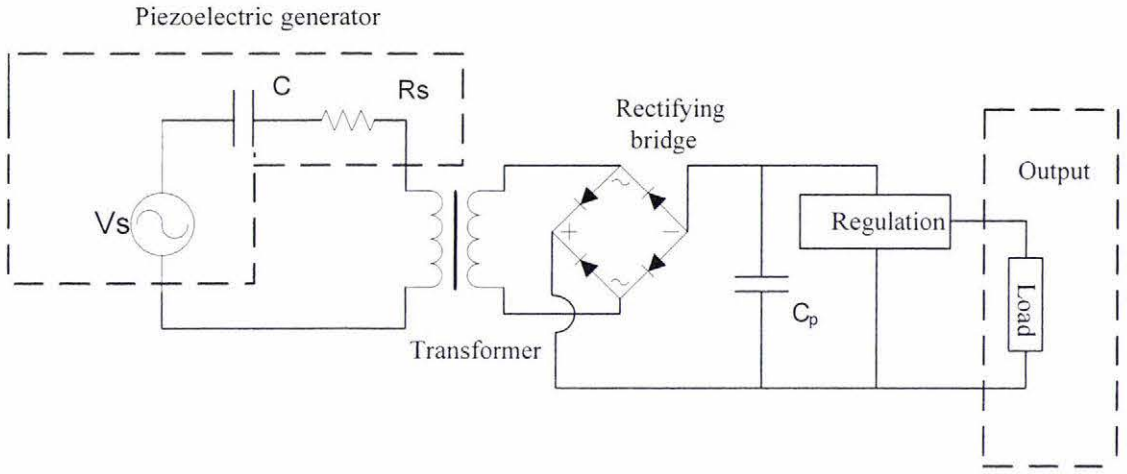


**Figure 5-1 Piezoelectric generator with power circuitry**

They are PZT generator device, transformer, rectifying bridge, power storage, regulation and output. From mechanical point of view, the piezoelectric generator acts as vibration-electricity converter, which mechanical vibrations are converted into mechanical stress via a cantilever beam and the stress is converted into electrical charge through the use of a piezoelectric material. From electrical point view, the piezoelectric generator is treated as the combination of current source and capacitor. The voltage converted is around 230 volt by calculation, so the transformer gives 1:3 ratio of conversion which is approximately 80 volts of AC voltage. The electric charge must then be rectified. A rectifier converts a sinusoidal voltage to a constant voltage. Here a full-wave rectifier is used in the circuit. The full-wave rectifier allows both halves of the AC phase to get through either the positive or negative cycle of voltage. This would produce more energy as the output than actually required. Therefore, the circuit with the full-wave rectifier is more efficient than the half-wave rectifier.

The AC voltage generated from the piezoelectric source is full-wave rectified through 1-A diode bridge. As the generator device powers up, the charge is transferred into electrolytic bucket capacitor Cp during the vibrating period of the beam.

Before feeding the voltage to power consumer the electric charge needs to be regulated so that it can provide constant and stable DC output voltage. The output voltage would continuously holds at the specified level regardless of changes in load

current or input voltage. In this case study a magnetic wireless sensor is treated as a load resistance connected at the end of the circuit. Therefore, the regulator supplies 5 volts of DC voltage environment for the wireless sensor to work. However, in this application size and efficiency are critical. LM2671-5 regulator or switch mode regulator may be chosen to regulate the voltage before feeding into the output, because it has a fairly high efficiency at relatively high output. In comparison to the above regulator, linear voltage regulators are inefficient. The linear regulators have to dissipate a large amount of power so that a large amount of heat is generated. They have to be adequately cooled, by mounting them on heatsinks. This results in making the regulator bulky and large.

LM2671-5 regulator overcomes the drawbacks of linear regulators. Switched power supplies are more efficient and they tend to have an efficiency of 90%. They can step up or step down the input voltage and can be packaged in a fraction of the size of linear regulators.

### 5.3. Conclusion

A classic AC-DC converter circuit was built that provides constant and stable 5 volts DC to the output. A schematic of the power circuit is shown in Figure 5-2. Once the schematic circuit diagram is completed, the final PCB board of the circuit was made as shown in Figure 5-3 and Figure 5-4.

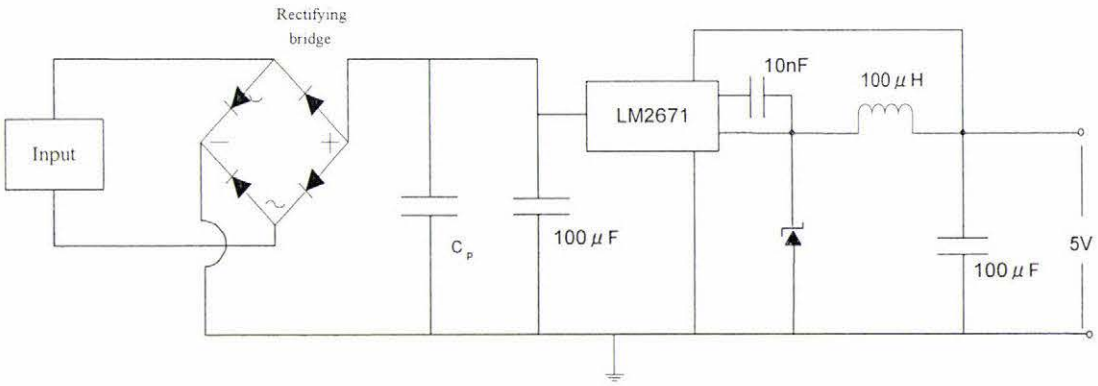


**Figure 5-2 Schematic diagram of power supply circuitry**

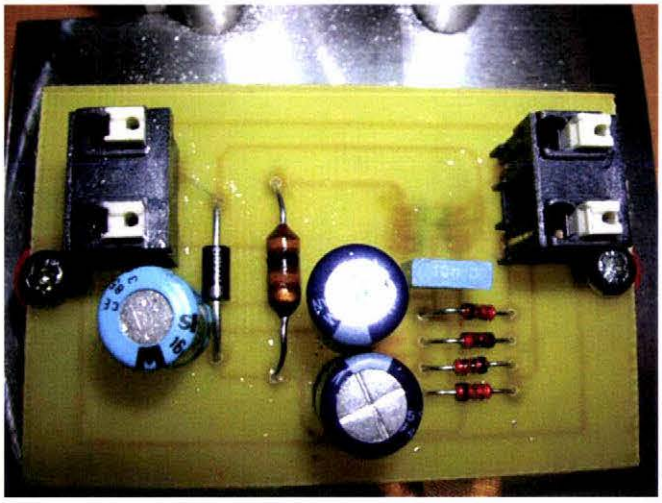

**Figure 5-3 Top view of the PCB circuit board**

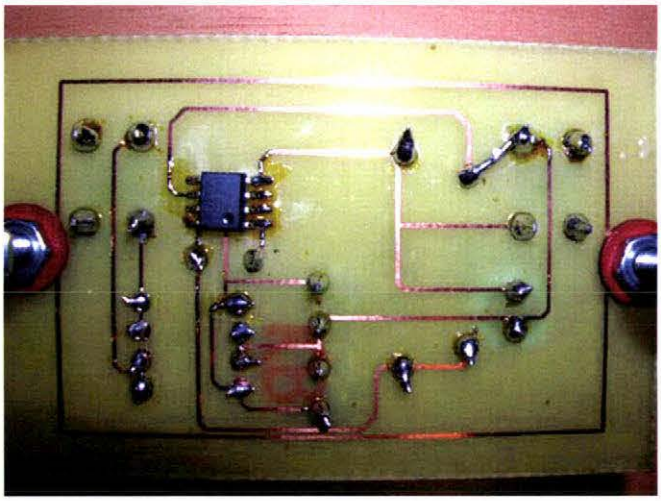

**Figure 5-4 Bottom view of the PCB circuit board**

# 6. Experimental studies of prototyped power generator

## 6.1. Experimental setup

Once the mathematical model of the design is finished and the optimization is completed the experimental setup of the case study is feasible. The piezoelectric material (PSI-5H4E) with nickel electrodes is purchased from Piezo System Inc. The reason of the material selection is given in Chapter 3. Single sheet piezoceramics is very fragile and it has to be tailored into two pieces of required size piezoceramics.

On the other hand, the supplier suggests two piezo sheets be bonded together with either brass or stainless steel shim between them and then they become rugged enough not to be damaged when it drops accidentally. In this case a brass shim is used to joint two pieces of tailored PZT. Also a tool steel mass with 7.715 $cm^3/g$ density is stuck at one end of the PZT. The dimensions of the piezoelectric device are based on the Table 4-3.

In order to make a cantilever beam a plastic table with a step is built and one end without mass of the 2-Layer piezoelectric bending element is clipped in the table. A 30 gauge wire or smaller is recommended to minimize strain on the solder joint during wire handling. The cantilever beam is shown in Figure 6-1.

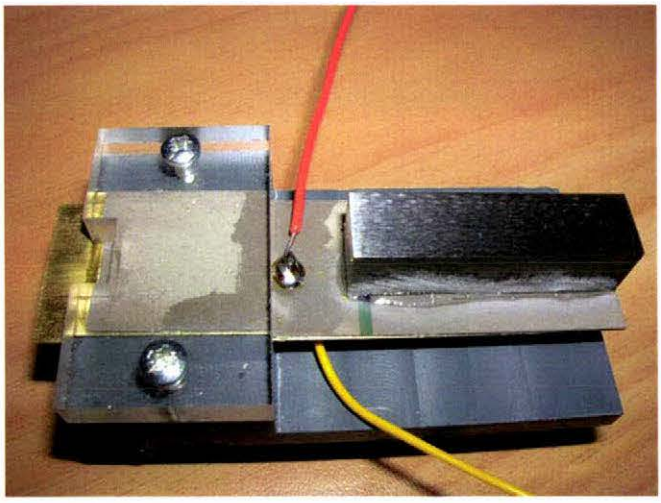

**Figure 6-1 Piezoelectric generator prototype**

As mentioned in Chapter 4 the cantilever beam should be working in a vibration source of $0.05m/s^2$ at 25 Hz. Therefore, a simulated environment is necessary for the

experiment. The frequency and the acceleration of input vibration are generated by eccentric dick rotated by a DC motor. A vibration table consists of a DC motor, a slice of round aluminium and a square aluminium base with four holders supporting the generator device, as shown in Figure 6-2. The vibrating frequency with 25 Hz is achieved by calculating angular speed of the DC motor. This speed can be adjusted to the specified value when changing the feeding voltage through a power generator. Figure 6-3 shows a revolution meter that is used to measure the rotational speed in revolution per minute (RPM). RPM is a unit of frequency, which 1 r/min = 0.01666667 Hz. The measured frequencies are decided according to the feeding voltage of the DC motor from 3V up to 9V with an incremental interval of 1V except 8.3V for possible resonant frequency (Table 6-1).

**Table 6-1 Motor feeding voltage vs. frequency**

| Voltage generator (DC) | Frequency (Hz) |
|---|---|
| 3V | 7 |
| 4V | 10 |
| 5V | 12 |
| 6V | 15 |
| 7V | 18 |
| 8V | 22 |
| 8.3V | 25 |
| 9V | 31 |

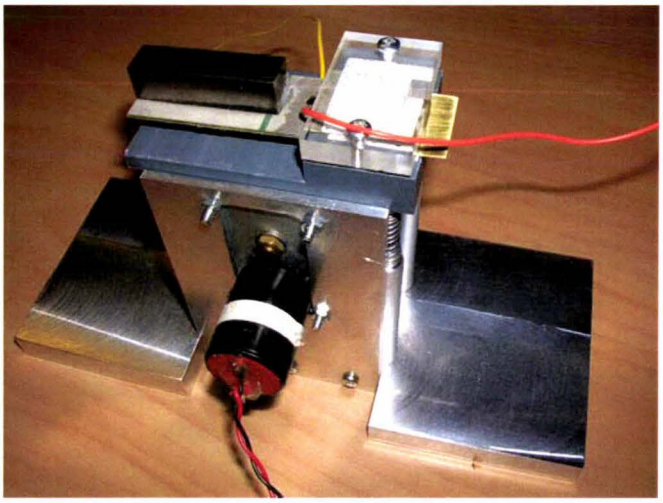

**Figure 6-2 Vibration table with PZT generator**

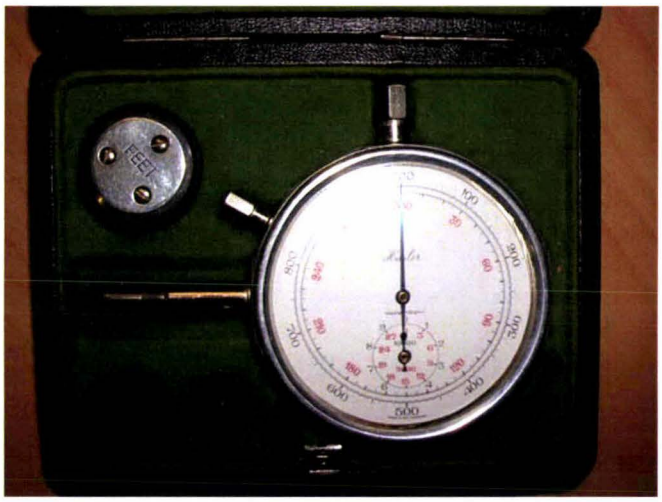

**Figure 6-3 Revolution meter**

For the acceleration, it is defined as the second derivative of position, which is represented by.

$$A = \frac{d^2 x}{dt} \tag{6.1}$$

which x is the displacement, for this case, it also can be rewritten as,

$$A = x \cdot \omega^2 \cdot \cos(\omega \cdot t) \tag{6.2}$$

The amplitude of the input vibration is controlled by altering the eccentric distance of the disk. There are three round disks prepared for this experiment. The maximum vertical displacement of the beam is considered when designing the eccentric disks. It can be calculated below.

$$D_{\max} = \frac{S_{\max} L^2}{4t_c} \tag{6.3}$$

which $S_{\max}$ is maximum surface strain, L is the length of the cantilever beam and $t_c$ is the thickness of the beam. The maximum surface strain of PZT is 500 microstrain [23]. Therefore, the maximum vertical displacement is 1.6mm in this case. Three round disks are machined and have different offsets of eccentricity at 1.5mm, 1mm and 0.5mm.

## 6.2. Experimental plan and procedure

The purpose of the experiment is to find out the performance of the measured power output and voltage versus driven frequency, load resistance versus peak voltage, acceleration versus power output and also to measure mechanical damping ratio. Some of the measured results are also compared with the simulated data. All the experiments are performed with an acceleration magnitude of using the disk of eccentricity of 1.5mm. All the running results are recorded in the oscilloscope.

### *6.2.1. Output peak voltage vs. input frequency*

It is important to find the relationship between the voltage and input frequency at the beginning of the experiment as the maximum voltage will occur when the driven frequency matches the resonant frequency. There are five measurements to be taken for each frequency as mentioned in Chapter 6.1. The averaged value is used as the final result. As an outcome of the experiment, the resonant frequency should be found. The connection of this experiment is shown in Figure 6-4.

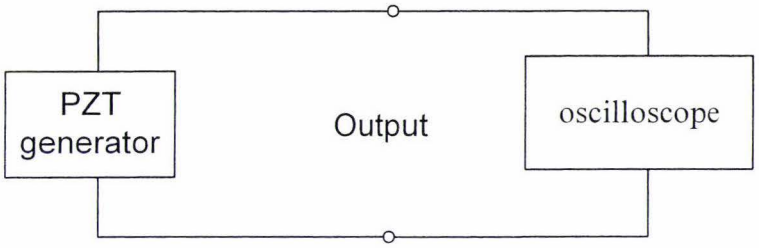


**Figure 6-4 Output voltage vs. input frequency circuit diagram**

### *6.2.2. Load resistance vs. output power*

This experiment is implemented below the resonant frequency by changing the load resistance to seek the maximum peak voltage. By calculation, the optimal resistance is around 350 kΩ. Therefore, there are some resistance directly connected to the output and it is expected one resistance load with around 350 kΩ has a maximum peak voltage. The circuit diagram is shown in Figure 6-5. In this stage the output power can be calculated in equation $P = V^2/R$. The relationship between load resistance and output power is gained as well.

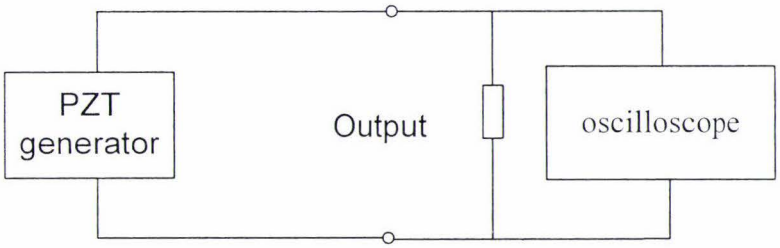


**Figure 6-5 Load resistance vs. peak voltage circuit diagram**

### *6.2.3. Mechanical damping ratio measurement*

The damping ratio can be measured by applying an impulse to the system and measuring the output. The damping ratio then was calculated as a function of the log decrement of the two magnitudes, and the number of periods as [41].

$$\zeta = \frac{1}{2\pi n} \ln\left(\frac{x_1}{x_2}\right) \qquad (6.4)$$

where $x_1$ is the magnitude at one point of the damped oscillation, and $x_2$ is the magnitude of the damped oscillation n periods later. Several measurements will be taken.

### *6.2.4. Output power vs. input frequency*

In experiment 6.2.2 the optimal load resistance is found, so this experiment is implemented by changing the input frequency and recording the corresponding output voltage under the optimal load resistance. Then the output power is calculated towards the peak voltage and resistance. It is expected that the maximum output power and output peak voltage occur when the resonance frequency is reached. The circuit diagram used is the one shown in Figure 6-5.

### *6.2.5. Input acceleration amplitude vs. power output*

This experiment is run with optimal load resistance and resonant frequency. The input acceleration amplitude is adjusted by changing three eccentric round disks. Several output voltages are measured for each mass. The circuit diagram is same as the one in Figure 6-5, and only the disks are altered.

### *6.2.6. Experiments on circuit board*

The circuit board is used to converter the AC voltage to required DC voltage and save the power for supplying the wireless sensor. For this experiment, after full wave rectified, the peak output voltages are measured for five times at a frequency below the resonant frequency. Also there is a capacitor connected on the end of the circuit for storing the energy. The measurement of the voltage of the capacitor is taken. The saved energy is calculated by

$$E = \frac{1}{2} C V^2 \qquad (6.5)$$

The measured energy and the simulated power energy are compared, and for simulated situations, a small fan is driven by the PZT device.

### 6.3. Experimental results and analysis

During the experiment there was an accident when doing experiment on 6.2.1 which seeks the relationship between output peak voltage and input frequency. Basically the experiment was looking for a parabola curve which has a vertex when the input frequency meets the natural frequency of the PZT device. However, it resulted in cracking the piezoelectric material due to the ever increasing vibration. There were two cracks, one of which is on the top and the other at the bottom, shown in Figure 6-6 and 6-7, respectively. The cracked device could no longer operate to arrive at the designed performance.

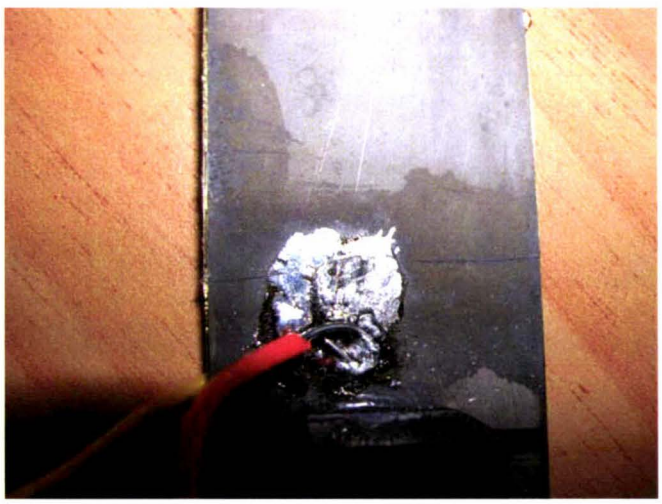

**Figure 6-6 Top of the cracked PZT device**

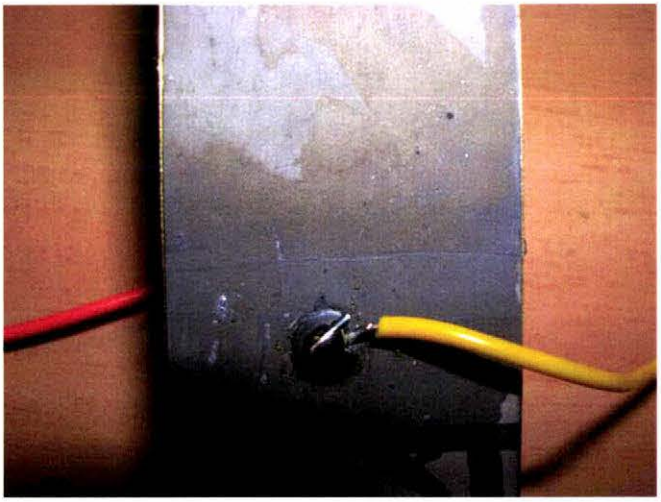

**Figure 6-7 Bottom of the cracked PZT device**

One of the solutions is to move the PZT device further into the clipper of the cantilever beam. Therefore, the cracked part of the PZT device can be ignored the modified device is shown in Figure 6-8. The reduction is 4mm, so the total of the cantilever beam is 44.5mm and the fundamental frequency is increased to around 30 Hz by calculation. Therefore, the further experiments were implemented using the modified device. Consequently, the experimental results were divided into two parts: before cracked and after cracked which is given in more details.

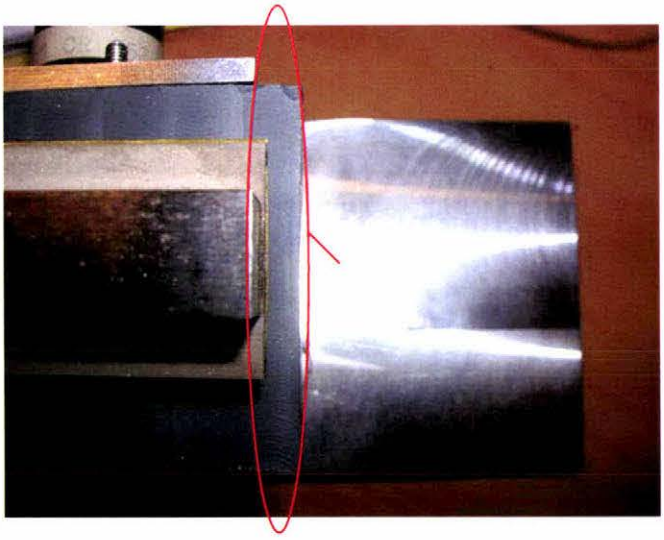

**Figure 6-8 Adjusted PZT device**

A. Before cracked

In terms of Equation (3.35), when the frequency of input vibration is equal to the undamped natural frequency, the maximum output power will occur. Therefore, finding out the resonance frequency is the most important task in the experiment. By calculation the theoretical resonance frequency is at 25 Hz which requires a feeding DC voltage of 8.3V according to Table 6-1. The sequence of the running DC voltage is 8.3V, 9V and 8V. The running result is given in Table 6-2.

**Table 6-2 Output voltage vs. frequency before cracked**

| Feeding voltage (DC) | Frequency | Output voltage (Pk-Pk) |
|---|---|---|
| 8. 3V | 25Hz | 206V |
| | | 208V |
| | | 200V |
| 9V | 30Hz | 150V |
| | | 152V |
| | | 166V |
| 8V | 22Hz | 244V |
| | | 238V |
| | | 244V |

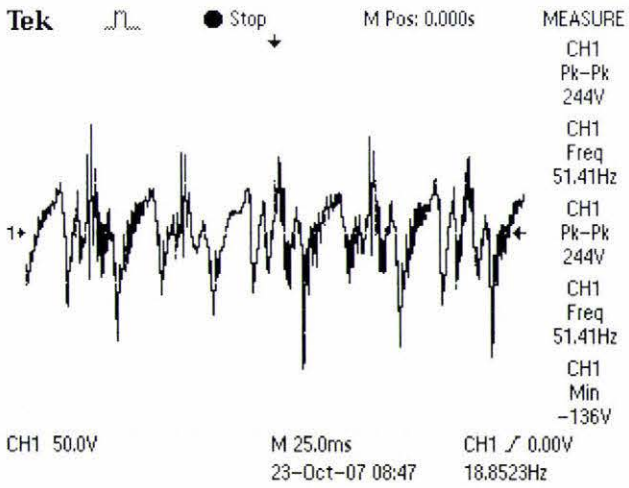


**Figure 6-9 Voltage behaviour at 22 Hz before cracked**

However, when the motor is driven at 8V, the cantilever beam vibrates very severely and the output peak-peak voltage is increased dramatically. After several times of

vibration, the cantilever beam (of piezoelectric materials) is cracked and the voltage output then drops to a very low level. Therefore, the resonance frequency was assumed at 22 Hz which is very close to the theoretical resonance frequency 25 Hz.

B. After cracked

After cracked, the length of the cantilever beam was reduced 4mm as shown in Figure 6-8. The rest of the experiments were implemented under the adjusted PZT device.

### *6.3.1. Output peak voltage vs. input frequency*

This experiment was redone after the device was adjusted. The procedure was similar as previous, but for safety purpose, the sequence of feeding voltage is set 3V, 4V, 5V, 6V and 7V (frequency from 7 Hz up to 18 Hz) while even the fundamental frequency of the cantilever beam was increased. Each situation was run in several times and the results were averaged value as the final result. The results of the experiment are shown in Figure 6-10.

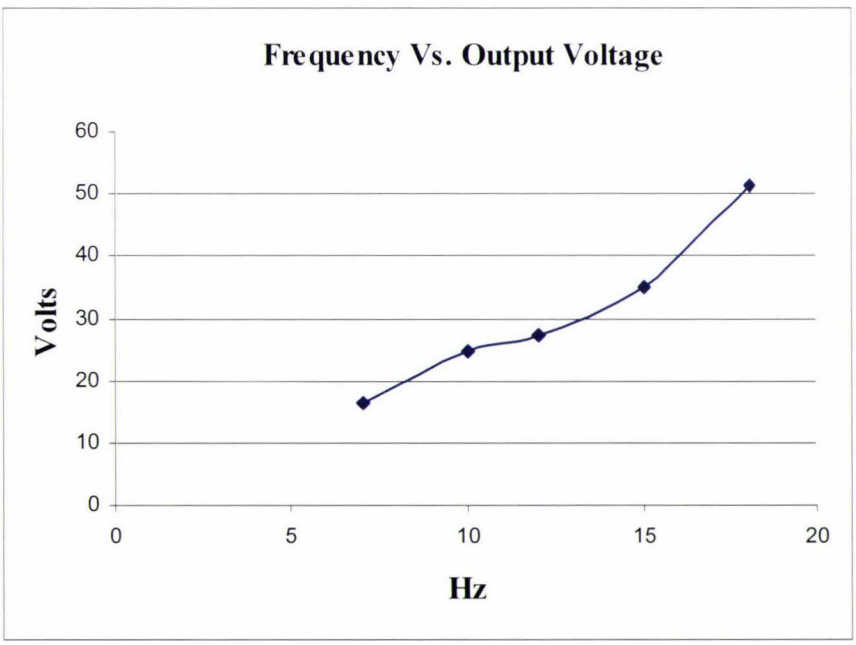


**Figure 6-10 Frequency versus output voltage after cracked**

The maximum voltage output is 52 Volts when input vibration frequency is 18 Hz. However, the resonance frequency of the cantilever beam is 28 Hz by calculation. It

seems that the result is much lower than that before cracked as the sizes of the cantilever beam is not optimal and did not reach the resonance frequency.

### *6.3.2. Load resistance vs. output power*

The circuit connection is shown in Figure 6-5. The resistance was inserted into a circuit demonstration board. The input vibration frequency is always run at 18 Hz. The tested resistances were 240 kΩ, 270 kΩ, 300 kΩ, 330 kΩ, 350 kΩ, 370 kΩ, 390 kΩ, 410 kΩ and 470 kΩ. The running results and one of the measured voltage with 350 kΩ resistance are shown in Figure 6-11 and Figure 6-12.

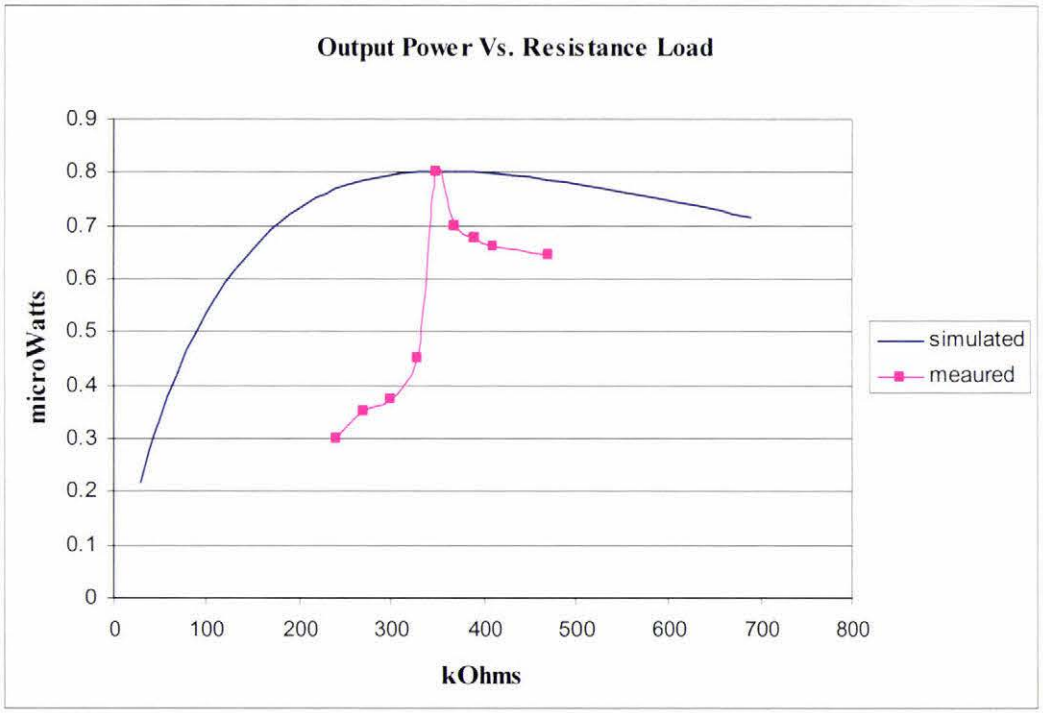


**Figure 6-11 Measured and simulated output power versus resistance load**

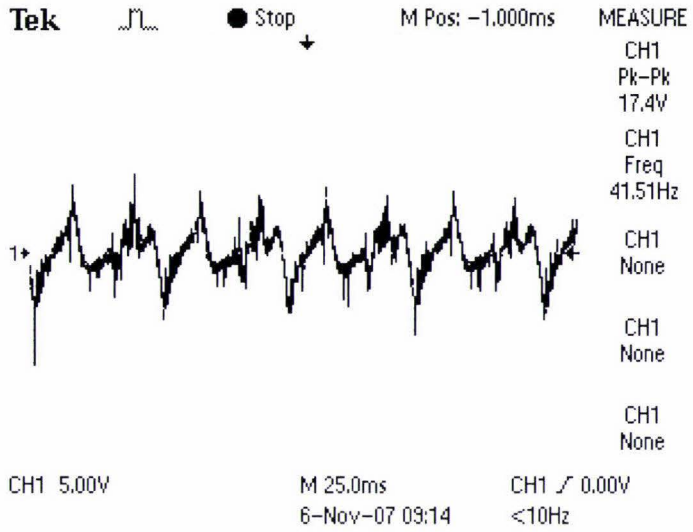


**Figure 6-12 Measured output voltage with resistance at 350 kΩ**

According to simulation and measurement, the optimal resistance load is 350 kΩ and the maximum power output is 0.8 mW.

### *6.3.3. Mechanical damping ratio measurement*

The damping ratio can be measured by applying an impulse to the system and measuring the output. The output result is shown in Figure 6-13. The x-coordinate represents time in second and the y-coordinate represents the magnitude of the damped oscillation. The magnitude of oscillation of the first point is 60.6 and after 3 periods apart the magnitude of oscillation is 25.9. Then the damping ratio is 0.045 by calculated in Equation (6.4).

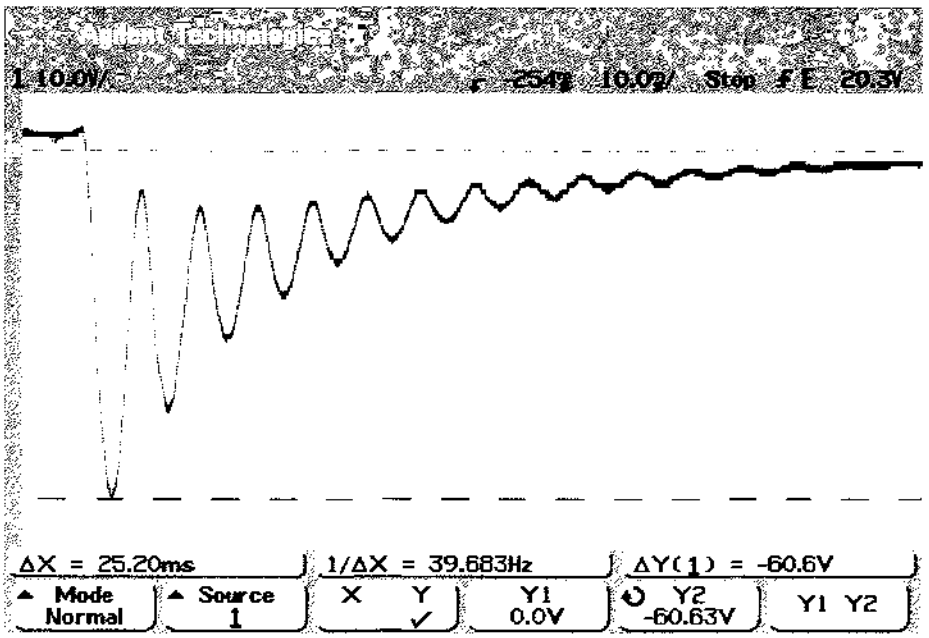


**Figure 6-13 Damped oscillation of PZT cantilever beam**

### *6.3.4. Output power vs. input frequency*

This experiment is based on experiment 6.3.2 which has found out the optimal resistance 350 kΩ. With changing the input vibration frequency from 7 Hz up to 18 Hz, the output voltage was increasing and recorded by oscilloscope. At each frequency the output voltage was run for three times, and then took the mean value. The result of the experiment is shown in below.

**Table 6-3 Output power versus input frequency**

| Input frequency (Hz) | Voltage output (V) | Power output (mW) |
|---|---|---|
| 7 | 7.73 | 0.170722571 |
| 10 | 13.07 | 0.488071143 |
| 12 | 13.93 | 0.554414 |
| 15 | 14.47 | 0.598231143 |
| 18 | 16.73 | 0.799694 |

It is easy to calculate the power when the voltage and the resistance are known from Table 6-3. It's obvious that the same power output as experiment 6.3.2 was 0.8 mW when the input frequency was 18 Hz.

### *6.3.5. Input acceleration amplitude vs. power output*

The acceleration magnitude of input vibrations is one of the most important factors affecting the output power. This experiment is implemented with optimal load resistance 350 kΩ at 18 Hz. In order to prevent the cantilever beam from being broken, the maximum displacement of the vibration is calculated in Equation (6.3). There are three eccentric disks tested in turn: 0.5mm, 1mm and 1.5mm. The running results are shown in Figure 6-14.

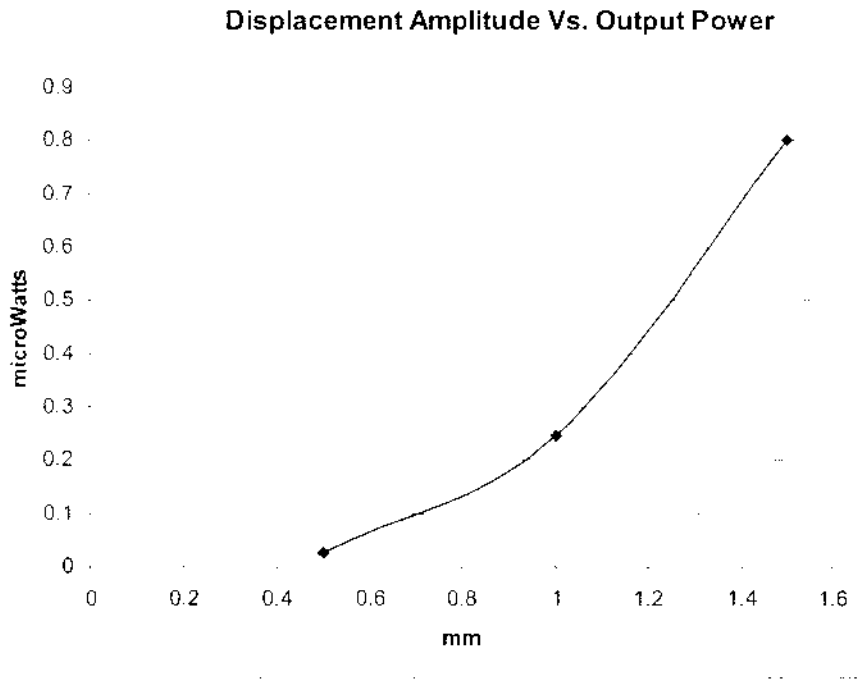


**Figure 6-14 Displacement amplitude versus output power**

It is clear that the output power went up dramatically each time when increasing 0.5mm displacement amplitude. It also can be explained in Equation (3.35) where vibration acceleration amplitude affects the output power in a square factor.

### *6.3.6. Experiments on circuit board*

The purpose of the circuit board is to rectify AC voltage, save energy, regulate voltage and supply stable 5V DC output. The PCB board has been built and mounted on the vibration table, as shown in Figure 6-15. There are three sub-experiments in the circuit board test. They are rectifier detection, energy storage and final output.

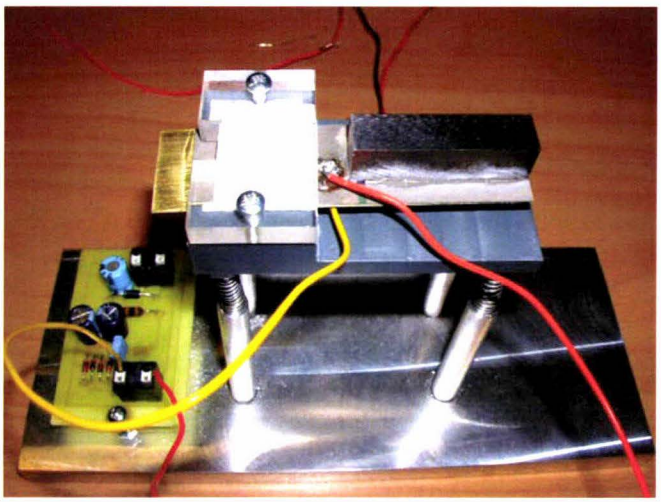

**Figure 6-15 Circuit board mounted on the vibration table**

The first experiment on the PCB is to detect the signal after rectifier which is composed by four diodes. The result is shown in Figure 6-16.

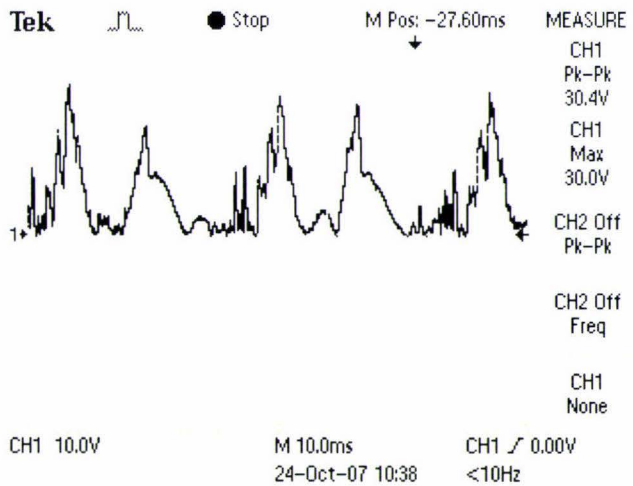


**Figure 6-16 Rectified output signal from PCB board**

From the figure above, it is shown that a full wave rectified signal is obtained and the peak voltage is half of the full AC voltage. The mean value over five times of this experiment is 26.88 V.

The second experiment is to test how long it takes to fully charge a specified capacitor full and how much energy could be stored in the capacitor. Based on the previous experiment the output voltage after rectified is around 30 V. Therefore, the required capacitor for test should be higher and close to 30 V. Also the capacitor that has large capacity and small size is preferred. In terms of the requirement a capacitor with 1000uF at 50 V is suitable in the case study. Two capacitors, 1000uf and 2000uF at 50 V, were compared in order to explore the charging capability of the generator. The capacitors were parallel behind the rectifier, as shown in Figure 6-17.

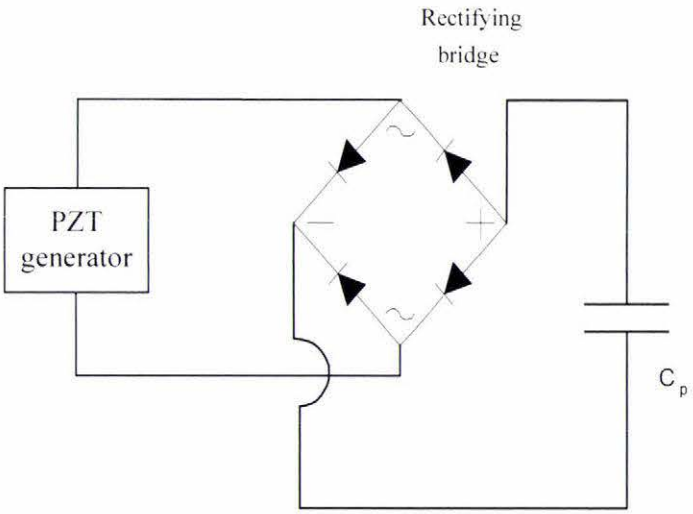


**Figure 6-17 Capacitor charge circuit diagram**

The running results were recorded at 5 minutes, 10 minutes, 15minutes, etc until the capacitor was fully charged or close to a full charge. Parts of the experiment results were shown in below.

**A. 1000uF**

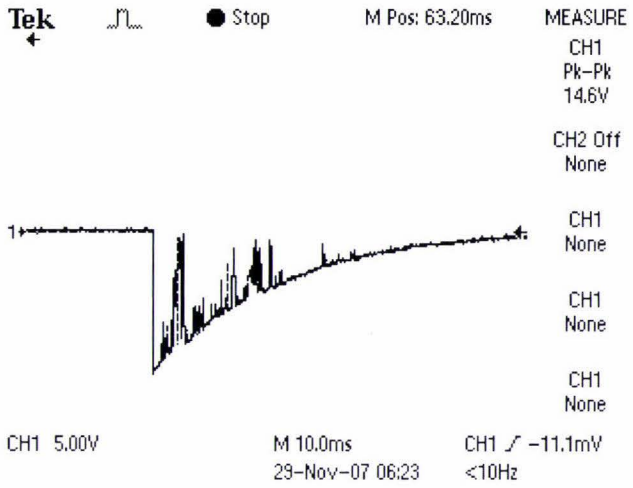


**Figure 6-18 Capacitor charged for 5 minutes**

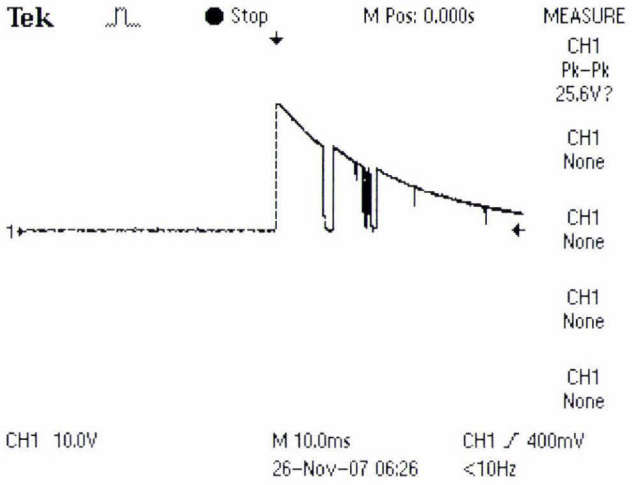


**Figure 6-19 Capacitor charged for 15 minutes**

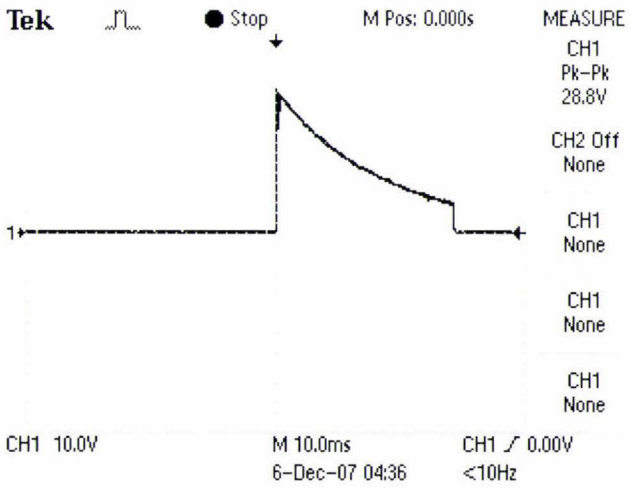


**Figure 6-20 Capacitor charged for 15 minutes**

According to the previous experience the output voltage after rectifier was up to 30 V. Therefore, this experiment was stopped at this stage and summarized in Table 6-4.

**Table 6-4 1000uF capacitor charge summary**

| 1000uF | | |
|---|---|---|
| **Time** | **Peak voltage (Volts)** | **Power Saved (Watts)** |
| **5min** | 14.7 | 0.108045 |
| **10min** | 23.6 | 0.27848 |
| **15min** | 28.8 | 0.41472 |

Based on the experimental result, the total charging time required for the wireless sensor is shown in Table 6-5.

**Table 6-5 1000uF capacitor charge time for wireless sensor**

| 1000uF | | |
|---|---|---|
| **Time** | **Power Saved (Watts)** | **Hours Required** |
| **5min** | 0.108045 | 15.27141469 |
| **10min** | 0.27848 | 11.85004309 |
| **15min** | 0.41472 | 11.93576389 |

**B. 2000uF**

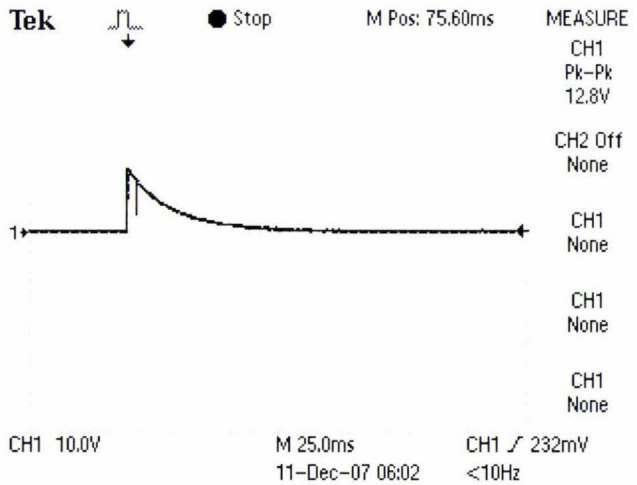


**Figure 6-21 Capacitor charged for 5 minutes**

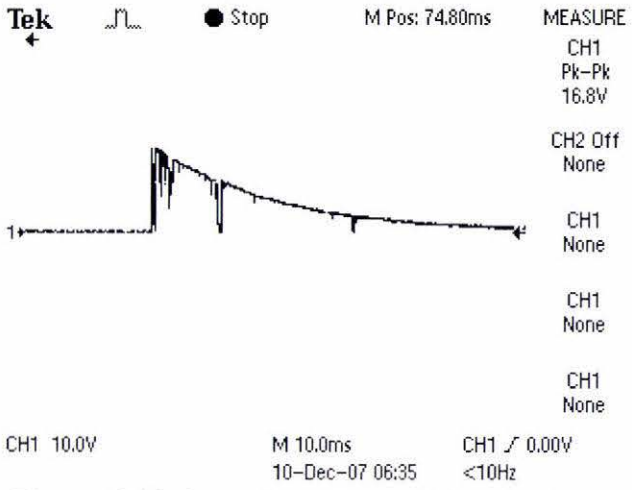


**Figure 6-22 Capacitor charged for 10 minutes**

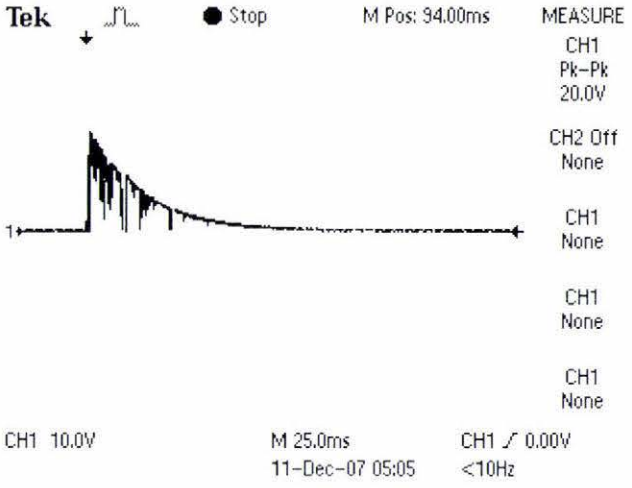


**Figure 6-23 Capacitor charged for 15 minutes**

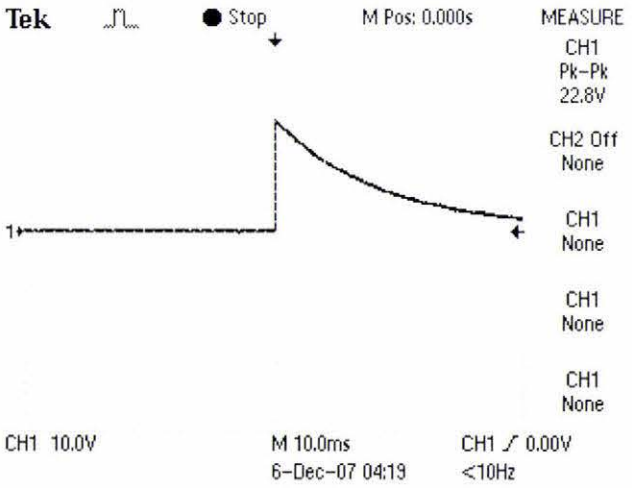


**Figure 6-24 Capacitor charged for 20 minutes**

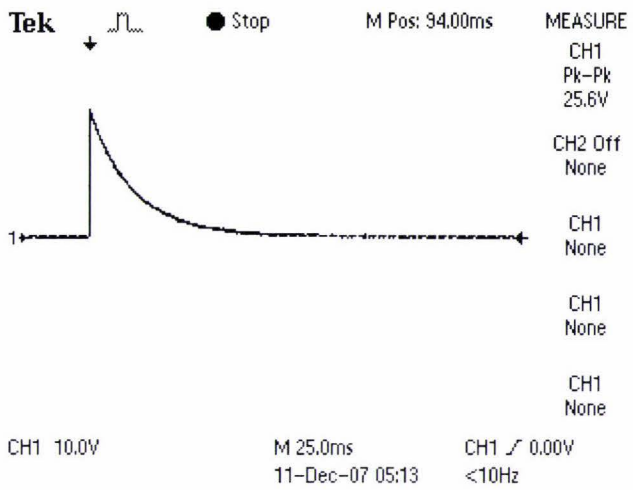


**Figure 6-25 Capacitor charged for 25 minutes**

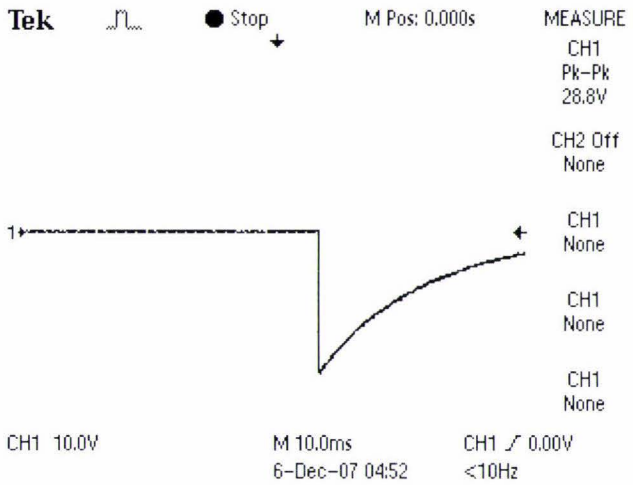


**Figure 6-26 Capacitor charged for 30 minutes**

This experiment was implemented until being charged for 30 minutes. The summary of the testing results is shown in Table 6-6 and the charging time is given in Table 6-7.

**Table 6-6 2000uF capacitor charge summary**

| 2000uF | | |
|---|---|---|
| **Time** | **Peak voltage (Volts)** | **Power Saved (Watts)** |
| **5min** | 11.3 | 0.12769 |
| **10min** | 15.9 | 0.25281 |
| **15min** | 20 | 0.4 |

| | | |
|---|---|---|
| **20min** | 23.6 | 0.55696 |
| **25min** | 25.6 | 0.65536 |
| **30min** | 28.8 | 0.82944 |

**Table 6-7 2000uF capacitor charge time for wireless sensor**

| 2000uF | | |
|---|---|---|
| **Time** | **Power Saved (Watts)** | **Hours Required** |
| **5min** | 0.12769 | 12.92192028 |
| **10min** | 0.25281 | 13.05328112 |
| **15min** | 0.4 | 12.375 |
| **20min** | 0.55696 | 11.85004309 |
| **25min** | 0.65536 | 12.58850098 |
| **30min** | 0.82944 | 11.93576389 |

The charging experiments have showed that the PZT generator could generate around 0.026 Watts/min (saved in the capacitor). In other words, there should need approximately 13 hours for the energy to be saved into the capacitors for the consumption of the wireless sensor.

Once the energy is saved into the capacitor, the next step is to use the power to supply the load (or wireless sensor). In order to provide stable and suitable voltage to the load, a good regulator is needed, which has been already detailed in Chapter 5. Therefore, the third experiment is to examine the circuit output after regulator. The experiment is implemented and shown below.

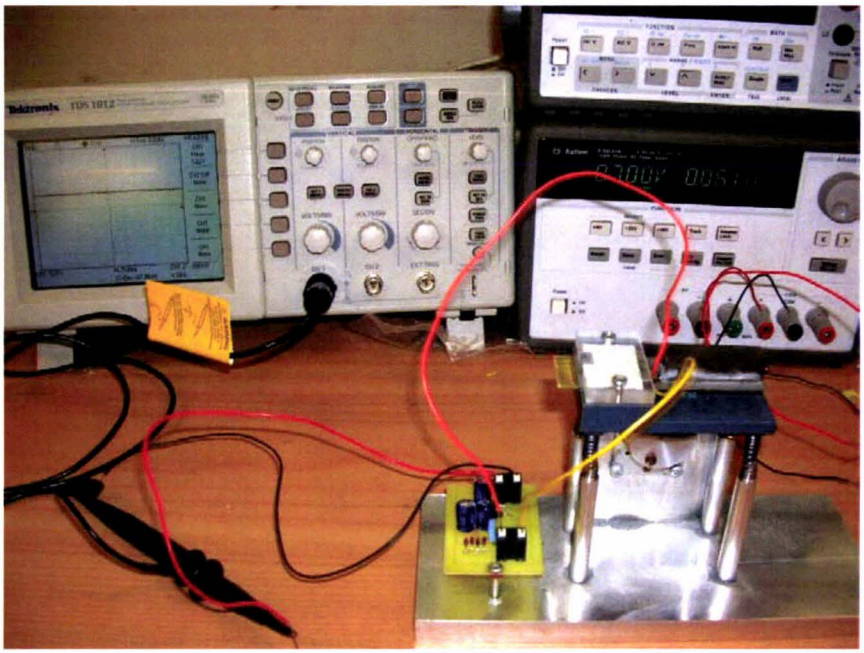

**Figure 6-27 Implementation of PZT generator with power circuit**

For the sake of saving time, there were only two 100uF capacitors used in the storage circuit. After running for five minutes, a 5 Volts DC was got by oscilloscope, as shown in Figure 6-28.

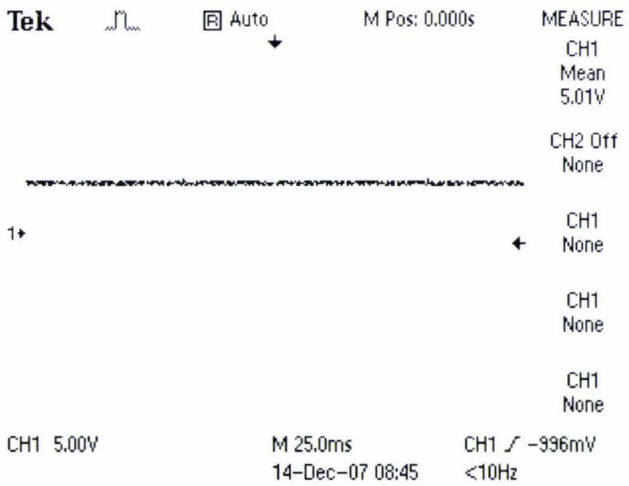


**Figure 6-28 5 Volts DC output**

This proves that the PZT generator could provide a stable 5 Volts DC output via power circuit. A further experiment was to connect a little 5 V DC fan at the output end of the circuit. It is expected that the generated power can turn the fan.

However, the fan did not turn after PZT power generator was vibrated for more than 10 minutes. The reason is that the fan consumes 5V*0.12A = 0.6W and 0.6W*1sec =

0.6J energy. but the maximum voltage of the 200uF capacitor is less 30 V. which means the maximum energy storage of the capacitor is $P = 1/2*C*V^2 = 0.09J$. Therefore. if the two capacitors are of 2000uF and the generator runs for a longer time. the stored energy could rotate the fan. However. the PCB board was designed for two medium size capacitors. if it changes to using larger capacitors or more parallel capacitors. a new PCB is required.

All in all. the purposes of the experiment have been successfully achieved and it has been validated that the PZT generator can provide a stable 5 V DC output for the 5 V low power wireless sensor.

# 7. Conclusions and recommendation

## 7.1. Conclusions

After a board survey of potential power sources for wireless sensor networks, low level vibration is chosen to scavenge energy for wireless sensor. The thesis work has contributed in the following.

First, based on the work by Roundy et al [1] a piezoelectric generator is modelled mathematically and simulated for analysis. It is shown that the mathematical expression Eq.(3-35) is suitable for PZT generator at low frequency vibration. The key factors which affect the generated power by PZT material are analysed.

Second, a wireless traffic monitoring sensor is assumed to be powered by piezoelectric generator. A PZT generator based on cantilever beam is designed specifically, which is then optimized in SQP.

Third, an AC-DC circuit for power storage is designed. The power circuit is composed of rectifier which is made of four diodes, energy storage which is made of paralleled capacitors, and regulator which is a LM2671 chip, high efficiency 500mA step-down voltage regulator.

Fourth, according to the designed and optimized PZT generator, a vibration table as a vibration source and a cantilever beam with PZT are made. The circuit diagram is implemented by PCB mounted atop the vibration table. Also comprehensive experiments are conducted and the results are analyzed. Capacitors 1000uF and 2000uF are examined to see how much energy could be generated by the PZT device.

Finally, a stable 5 V DC output is secured. This proves that the prototype PZT generator is successfully developed that can provide sufficient energy for the wireless sensor node.

## 7.2. Recommendation

The design of the prototype PZT generator in this thesis is far from being perfect. There are still a number of issues that have to be addressed.

One of them is that as the PZT material is very brittle the PZT device should be operated at a vibration frequency much lower than the device's resonant frequency, and while purchasing PZT material, it should be tailored according to the design dimension by the supplier company.

To improve the testing accuracy of the PZT generator, the vibration table could be changed into a vibrometer that can provide more accurate vibration frequency and acceleration amplitude.

Another concern in this project is to experiment on practical applications. The power generator should be tested on the roadside or bridge to scavenge energy from the ambient environment in the future.

One further concern is that there should be more capacitors paralleled in the storage circuit to get sufficient power for a large load. An actual wireless sensor should be secured with which the prototype PZT generator could be experimented.

## 8. References

[1] Roundy, S., Wright, P. K., & Rabaey, J. (2004). *Energy Scavenging for Wireless Sensor Networks with Special Focus on Vibrations.* Boston, USA: Kluwer Academic Publishers. pp.1- 212.

[2] British Heart Foundation. (2002). *Pacemakers information for people with pacemakers, and for their family and friends.* Retrieved on 18th Dec 2006:

www.whri.qmul.ac.uk/cardiology/research/patients/docs/pacemakers.pdf

[3] Saphire Information Society Technologies. (2006). *Intelligent Healthcare Monitoring based on a Semantic Interoperability Platform.* Retrieved on 3rd Jun 2006:

www.srdc.metu.edu.tr/webpage/projects/saphire/deliverables/SAPHIRED3.1.1_SOA_0.5.doc

[4] Mercy Hospital. (2004). *Mercy Hospital First in The Nation to Offer Patients Wireless ECG Monitoring.* Retrieved on 3rd Jun 2006:

www.mercymiami.org/News_and_Events/Press_Release_4.asp

[5] Alive Technologies Pty. Ltd. (2006). *Blood glucose monitor.* Retrieved on 11th May 2006: www.alivetec.com/products.htm

[6] Roundy, S., Steingart, D., Frechette, L., Wright, P. K., & Rabaey, J. M. (2004). *Power Sources for Wireless Sensor Networks.* Berlin, Germany. Jan. 19-21.

[7] Warneke, B. A.. (2003). *Ultra-Low Energy Architectures and Circuits for Cubic Millimeter Distributed Wireless Sensor Networks.* Berkeley, Canada: University of California.

[8] Otis, B., Rabaey, J. A., (2002). 300μW 1.9GHz CMOS Oscillator Utilizing Micromachined Resonators. *Proceedings of the 28th European Solid State Circuits Conference in Florence Italy.* September 24 – 26, pp. 8-125.

[9] Stordeur, M., & Stark, I. (1997). Low Power Thermoelectric Generator – self-sufficient energy supply for micro systems. *16th International Conference on Thermoelectrics.* pp. 575 – 577.

[10] Shenck, N. S., & Paradiso, J. A. (2001). Energy Scavenging with Shoe-Mounted Piezoelectrics. *IEEE Micro*. Vol.21. pp. 30-41.

[11] Williams, C. B, & Yates, R.B. (1995). Analysis of a micro-electric generator for Microsystems. *Transducers 95/Eurosensors IX.* pp.369 – 372.

[12] Ajitsaria, J., Choe, S.Y., Shen, D., & Kim, D.J. (2007). Modeling and analysis of a bimorph piezoelectric cantilever beam for voltage generation. *Smart Materials and Structures.* Vol.16 (2), April, pp. 447-454(8).

[13] Umeda, M., Nakamura, K., & Ueha, S. (1996). Analysis of Transformation of Mechanical Impact Energy to Electrical Energy Using a Piezoelectric Vibrator. *Japanese Journal of Applied Physics.* Vol.35, Part1, No. 5B, May, pp. 3267-3273.

[14] Starner, T. (1996). Human-Powered Wearable Computing. *IBM Systems Journal.* Vol. 35, pp. 618.

[15] Kymissis, J., Kendall, C., Paradiso, J., & Gershenfeld, N. (1998). Parasitic Power Harvesting in Shoes. *Second IEEE International Conference on Wearable Computing.* pp. 132-139.

[16] Kimura, M. (1998). On the Efficiency of Electric Power Generation With Piezoelectric Ceramic. *Journal of Dynamic Systems, Measurement, and Control.* Vol. 121, pp 566-571.

[17] Clark, W., & Ramsay, M. J. (2000). Smart Material Transducers as Power Sources for MEMS Devices. *International Symposium on Smart Structures and Microsystems.* Hong Kong.

[18] Elvin, N.G., Elvin, A.A., & Spector, M. (2001). A self-Powered Mechanical Strain Energy Sensor. *Smart Materials and Structures.* Vol. 10, pp. 293-299.

[19] Elvin, N.G., Elvin, A.A., & Spector, M. (2000). Implantable bone strain telemetry system and method. *US Patent Specification 6034296.*

[20] Kasyap, A., Lim, J., Johnson, D., Horowitz, S., Nishida, T., Ngo, K., Sheplak, M., & Cattafesta, L. (2002). Energy Reclamation from a Vibrating Piezoceramic Composite Beam. *Proceedings of 9th International Congress on Sound and Vibration.* Orlando, FL, USA. July, 2002.

[21] Gonzalez, J. L., Moll, F., & Rubio, A. (2001). A prospect on the use of Piezoelectric Effect to Supply Power to Wearable Electronic Devices. *International Confereence on Materials Engineering for Resources.* Akita, Japan, October 2001, Vol.1, pp.202-207.

[22] Smits, J. G., & Choi, W. S. (1991). The constituent equations of piezoelectric heterogeneous bimorphs IEEE Trans. Ultrason. Ferroelectr. Freq.Control. Vol. 38(3) pp. 256-70.

[23] Piezo Systems, Inc. (2006). *Introduction to piezo transducers.* Retrieved on 27th Aug. 2007: http://www.piezo.com

[24] PI Ceramic GmbH. (2007). *The Piezoelectric Effect.* Retrieved on 29th Aug. 2007: http://www.piceramic.de/piezoeffekt.html

[25] Flynn, A. M., & Sanders, S. R. (2002). Fundamental limits on energy transfer and circuit considerations for piezoelectric transformers. *IEEE Transactions on Power Electronics.* vol.17 (1), Jan. pp.8-14.

[26] Texas Transportation Institute. (2006). *Urban Mobility Report, 2006.* Retrieved on 6th Nov. 2006: http://mobility.tamu.edu/ums/report/

[27] Middleton, D.R. & Parker, R.T. (2000). Initial Evaluation of Selected Detectors to Replace Inductive Loops on Freeways. *Texas Transportation Institute Technical Report.* April. pp. 1439-7,.

[28] Cheung, S. Y., Ergen, S. C., & Varaiya, P. (2005). Traffic Surveillance with Wireless Magnetic Sensors. *Proc. 12th ITS World Congress.* San Francisco, USA. Nov. 2005.

[29] Cheung, S. Y., Ergen, S. C., & Varaiya, P. (2004). *Sensor Networks for Monitoring Traffic.* San Francisco, USA. Aug. 2004.

[30] Levis,P., Madden, S., Gay, D., Polastre, J., Szewczyk, R., Woo, A., Brewer, E., & Culler, D. (2004). The Emergence of Networking Abstractions and Techniques in TinyOS. *First USENIX/ACM Symposium on Networked Systems Design and Implementation, 2004.*

[31] Tadiran Batteries. (2006). TL5135/SP Specifications. Retrieved on 6th Nov. 2006: http://www.tnrtechnical.com/Tadiran/TL5135P.htm

[32] Paradiso, J. A. & Starner, T. (2005). Energy scavenging for mobile and wireless electronics. *IEEE Pervasive Computing.* Vol. 4 (1), Jan.-March. pp.18-27.

[33] Roundy, S., Leland, E. S., Baker, J., Carleton, E., Reilly, E., Lai, E., Otis, B., Rabaey, J. M., Sundararajan, V., & Wright, P. K. (2005). Improving power output for vibration-based energy scavengers. *IEEE Pervasive Computing.* Vol. 4 (1), Jan.-March. pp.28-36.

[34] Hunaidi, O. (2000). *Traffic Vibrations in Buildings.* Retrieved on 5th Mar. 2007):

http://irc.nrc-cnrc.gc.ca/pubs/ctus/39_e.html

[35] Powell, M. J. D. (1978). A Fast Algorithm for Nonlinearly Constrained Optimization Calculations, in: G. A. Watson (Ed.). *Proceeding of the 1977 Dundee Biennial Conference on Numerical Analysis.* Springer, Berlin, Germany, Vol. 630, pp. 144-157.

[36] Gill, P. E., Murray, W. & Wright, M. H. (1991). *Numerical Linear Algebra and Optimization.* USA: Addison Wesley.

[37] Gill, P. E., Murray, W., Saunders, M. A., & Wright, M. H. (1984). Procedures for Optimization Problems with a Mixture of Bounds and General Linear Constraints. *ACM Trans. Math. Software.* Vol.10, pp 282-298.

[38] Han, S. P. (1977). A Globally Convergent Method for Nonlinear Programming. *J. Optimization Theory and Applications.* Vol. 22, pp. 297.

[39] Chapman, P. L., & Krein, P. T. (2001). Micromotor Technology: Electric Drive Designer's Perspective, in *Proceedings 2001 IEEE Industry Application Society Conference.* Chicago, IL.

[40] Schwartz, R. W., Cross, L. E., & Wang, Q. M. (2001). Estimation of the Effective d31 Coefficients of the piezoelectric Layer in Rainbow Actuatoors. *Journal of the American Ceramic Society.* vol. 84 (11), pp. 2563-2569.

Niu, P., Chapman, P. L., Riemer, R., & Zhang, X. (2004). Evaluation of motions and actuation methods for biomechanical energy harvesting, in *IEEE Power Electronics Spec. Conference.* Vol. 3, pp. 2100-2106.

# APPENDIX

## Matlab Program for Optimization

```
function [c, ceq] = MaxCon(x)
Yc = 6.2e10;                % Young's modulus of PZT unit in N/m^2
Ysh = 9.02e10;              % Young's modulus of steel shim unit in N/m^2
Y = Yc/Ysh;
tp = 0.000267;              % Thickness of PZT
tsh = 0.000102;             % Thickness of shim
D = 320e-12;                % Strain coefficient
Ain = 0.005;
Dp = 0.02;                  % Damping ratio


P = 7715;                   % Mass desity unit in kg/m^3
Pb = 7800;                  % PZT desity unit in kg/m^3
L = x(1)+x(2);
V = x(2)*x(4)*x(5);
M = P*V;
Mb = Pb*(L*x(3)*2*tp);
I = x(3)*((2*tp^3+Y*tsh^3)/12 + 2*tp*(tp/2+tsh/2)^2);        % Inertia moment
T = 2*tp+tsh;
Smax = 5e-4;                % Maximum surface strain
deltaX = Smax*(x(1)+x(2))^2/T;          % Maximum deflection
Fc = 3*Yc*I*deltaX/(x(1)+x(2))^3;
Vol = 0.0328*0.0328*0.010414;

% Nonlinear inequality constraints
c = [(x(1)+x(2))*x(5)*(x(4)+tsh+tp*2)-Vol;(x(1)+x(2))*x(3)*(x(4)+tsh+tp*2)-
Vol;M*9.81-Fc];   % Volume limitation
%c = [M*9.81-F;x(1)+x(2)-0.0328;x(3)-0.0328;x(4)+tsh+tp*2-0.0104;x(5)-0.0328]
% Nonlinear equality constraints
% P = 9217.4;                % Mass desity unit in kg/m^3
% Pb = 7800;                 % PZT desity unit in kg/m^3
% L = x(1)+x(2);
% V = x(2)*x(4)*x(5);
% M = P*V;
% Mb = Pb*(L*x(3)*2*tp);
% I = x(3)*((2*tp^3+Y*tsh^3)/12 + 2*tp*(tp/2+tsh/2)^2);        % Inertia moment

ceq = [(sqrt(3*Yc*I/((M+0.24*Mb)*L^3)))/(2*pi)-25];          % Frequency limitation
```

```
function f = MaxObj(x)
Yc = 6.2e10;                    % Young's modulus of PZT unit in N/m^2
Ysh = 9.02e10;                  % Young's modulus of brass shim unit in N/m^2
Y = Yc/Ysh;
tp = 0.000267;                  % Thickness of PZT
tsh = 0.000102;                 % Thickness of shim
E0 = 8.8541878176e-12;          % Vacuum permittivity
De = 3800;
E = E0*De;
D = 320e-12;                    % Strain coefficient
Ain = 0.005;
Dp = 0.02;                      % Damping ratio
F = 25;                         % Input frequency
K = 0.33;                       % Coupling coefficient = 0.75*0.44
C = E*(x(1)+x(2))*x(3)/(tsh+tp*2);  % Equivalent capacitance
b = 1.5*(tp+tsh)*(x(1)+x(2))/(x(1)^2*(2*x(1)+1.5*x(2)));  % Geometric constant
R = 2*Dp/(F*C*sqrt(4*Dp^2+K^4));    % Optimal load resistance


f = -
R*C^2*(Yc*D*tp*b)^2*Ain^2/((F*E)^2*((4*Dp^2+K^4)*(R*C*F)^2+4*Dp*K^2*R
*C*F+2*Dp^2));



clear
x0 = [0.0234,0.01,0.0071,0.01,0.0018];          % Make a starting guess at the
solution
lb = [0.01,0.01,0.0071,0.01,0.0018];            % Set lower bounds
%ub = [0.0254,0.0254,0.0254,0.0254,0.0254];     % Set upper bounds
ub = [];
options = optimset('LargeScale','off');
options = optimset(options,'Display','iter');
[x, fval] = fmincon(@MaxObj,x0,[],[],[],[],lb,ub,@MaxCon,options)

[c,ceq] = MaxCon(x);



function [x,favl] = runfmincon(x0)

% Set up shared variables with OUTFUN
history.x = [];
history.fval = [];
searchdir = [];


x0 = [0.01,0.04,0.01,0.01,0.01];          % Make a starting guess at the solution0
%x0 = [0.01,0.01,0.03,0.01,0.05];
```

```
%x0 = [0.05,0.01,0.01,0.01,0.01];

%x0 = [0.02,0.01,0.03,0.01,0.03];
%x0 = [0.02,0.03,0.02,0.01,0.01];
%x0 = [0.01,0.01,0.02,0.02,0.02];
%x0 = [0.05,0.01,0.01,0.01,0.01];
lb = [0.01,0.01,0.01,0.01,0.01];              % Set lower bounds
ub = [];
%options = optimset('largescal','off');
options = optimset('outputfcn',@outfun,'display','iter',...
'largescale','off');
[x,favl] = fmincon(@MaxObj,x0,[],[],[],[],lb,ub,@MaxCon,options)



clear;

i=1;
x1 = 0.01;
x2 = 0.01;
x3 = 0.01;
x4 = 0.01;
x5 = 0.01;
favl(i)=0;

stepsize=0.01;

Vol = 0.0328*0.0328*0.010414;   % Volume
tp = 0.000267;                  % Thickness of PZT
tsh = 0.000102;                 % Thickness of shim
T = tsh + tp*2;


while ((x1+x2)*x5*(x4+T)<Vol) && ((x1+x2)*x3*(x4+T)<Vol) &&
((x1+x2)<0.0624)    % Test x1
   x0(1)=x1;
   while ((x1+x2)*x5*(x4+T)<Vol) && ((x1+x2)*x3*(x4+T)<Vol) &&
((x1+x2)<0.0624)  % Test x2
      x0(2)=x2;
      while ((x1+x2)*x3*(x4+T)<Vol) && (x3<0.0724)        % Test x3
         x0(3)=x3;
         while ((x1+x2)*x5*(x4+T)<Vol) && ((x1+x2)*x3*(x4+T)<Vol)   % Test x4
            x0(4)=x4;
            while ((x1+x2)*x5*(x4+T)<Vol)        % Test x5
               x0(5)=x5;
               x00(i,:)=x0;
               [xx(i,:),favl(i)]=runfmincon(x0);
               i = i+1;
               x5 = x5 + stepsize;
            end
```

```
            x5 = 0.01;
            x4 = x4 + stepsize;
        end
        x4 = 0.01;
        x3 = x3 +stepsize;
    end
    x3 = 0.01;
    x2 = x2 + stepsize;
  end
  x2 = 0.01;
  x1 = x1 + stepsize;
end

find(favl==min(favl))
find(favl==max(favl))



function stop = outfun(x,optimValues,state)

history.x = [];
history.fval = [];
searchdir = [];

    stop = false;
     switch state
       case 'init'
          hold on
       case 'iter'
       % Concatenate current point and objective function
       % value with history. x must be a row vector.
         history.fval = [history.fval; optimValues.fval];
         history.x = [history.x; x];
       % Concatenate current search direction with
       % searchdir.
         searchdir = [searchdir;...
                optimValues.searchdirection'];
         plot(optimValues.iteration,history.fval,'o');
         evalin('base',['r(' num2str((optimValues.iteration)+1) ')=' num2str(history.fval)
':']);
         evalin('base',['x1(' num2str((optimValues.iteration)+1) ')=' num2str(x(1)) ';']);
         evalin('base',['x2(' num2str((optimValues.iteration)+1) ')=' num2str(x(2)) ';']);
         evalin('base',['x3(' num2str((optimValues.iteration)+1) ')=' num2str(x(3)) ';']);
         evalin('base',['x4(' num2str((optimValues.iteration)+1) ')=' num2str(x(4)) ';']);
         evalin('base',['x5(' num2str((optimValues.iteration)+1) ')=' num2str(x(5)) ';']);
       % Label points with iteration number and add title.
         text(x(3),x(4),...
            num2str(optimValues.iteration));
         title('Sequence of Points Computed by fmincon');
       case 'done'
```

```
            hold off
        otherwise
    end
end
```